2008). Consequently, definitive diagnosis of neurodegenerative diseases is still reliant on post-mortem examination.

Post-mortem examination of the Alzheimer's disease brain is characterized by gross cortical atrophy (Wenk, 2003). Microscopically, Alzheimer's disease is characterized by the presence of extracellular β-amyloid plaques and intracellular neurofibrillary tangles (Wisniewski *et al.*, 1989; Ho *et al.*, 1994). There has been much progress in developing PET imaging radiotracers for the non-invasive detection of β-amyloid deposition (Shoghi-Jadid *et al.*, 2002; Klunk *et al.*, 2005; Rowe *et al.*, 2007, 2008; Choi *et al.*, 2009). Recent reports indicate that the best characterized and successful imaging agent Pittsburgh Compound-B (PiB), preferentially binds to fibrillar β-amyloid contained within cored and compact plaques (Klunk *et al.*, 2004; Maeda *et al.*, 2007; Ikonomovic *et al.*, 2008) and with much lower affinity to the oligomeric forms of β-amyloid (Maezawa *et al.*, 2008) that are thought to be the toxic species of β-amyloid in Alzheimer's disease (Lambert *et al.*, 2001; Walsh *et al.*, 2002; Ferreira *et al.*, 2007; Cairns *et al.*, 2009).

While amyloid imaging PET studies confirmed that β-amyloid deposition occurs well before the onset of symptoms (supporting the hypothesis that this represents preclinical Alzheimer's disease), these studies also showed the lack of correlation between β-amyloid plaque deposition and cognitive impairment in Alzheimer's disease; suggesting that markers for different and downstream effects of β-amyloid may be better suited to assess disease progression (Jack *et al.*, 2010). Therefore, new ligands are needed to explore alternative biomarkers as specific indicators of neurodegeneration. Such agents may prove invaluable in the diagnosis, follow-up and therapeutic monitoring of Alzheimer's disease and other dementias.

An obvious biomarker is tau and in particular, abnormal deposits of hyperphosphorylated tau as neurofibrillary tangles, neuropil threads and as dystrophic neurites surrounding β-amyloid plaques (a pathological hallmark of Alzheimer's disease); however, tau deposits are also characteristic of a larger group of neurodegenerative diseases termed tauopathies [i.e. sporadic corticobasal degeneration, progressive supranuclear palsy, Picks disease, as well as frontotemporal dementia and parkinsonism linked to chromosome 17 (FTDP-17)] (Lee *et al.*, 2001). Unlike β-amyloid plaque deposition, human post-mortem studies indicate that neurofibrillary tangle density correlates with neurodegeneration and cognitive impairment (Duyckaerts *et al.*, 1987, 1990; Delaere *et al.*, 1989; Arriagada *et al.*, 1992; Dickson, 1997; McLean *et al.*, 1999). Futhermore, abundant neurofibrillary tangles are not observed in cognitively unimpaired individuals, in contrast to β-amyloid plaques that are present in some non-demented people (Katzman *et al.*, 1988; Delaere *et al.*, 1990; Rowe *et al.*, 2007, 2008). Moreover, CSF-tau and phospho-tau (ptau181) have been proven useful biomarkers in the diagnosis of Alzheimer's disease (Blennow and Hampel, 2003; Ganzer *et al.*, 2003; Hampel *et al.*, 2009*a*, *b*).

Despite the quantitative assessment of CSF levels of tau and phospho-tau being reliable biomarkers of neurodegeneration (Jack *et al.*, 2010), lumbar puncture is an invasive procedure for the widespread screening of the at-risk population. Additionally, CSF measures do not provide information on regional brain tau deposition that may have clear correlates with cognition (i.e. hippocampus) and therefore, might not be able to provide important information on the therapeutic outcomes or response to current drugs aimed at modulating tau/neurofibrillary tangles (Gozes *et al.*, 2009; Hampel *et al.*, 2009*a*, *b*; Wischik and Staff, 2009).

Molecular neuroimaging with tau-specific radiotracers may provide highly accurate, reliable and reproducible quantitative statements of global and regional brain tau burden, essential for the evaluation of disease progression, therapeutic trial recruitment and the evaluation of tau-specific therapeutics (for both Alzheimer's and non-Alzheimer's disease taupathies); where tau plays a central role. Certainly, the viability of imaging disease-specific traits has been demonstrated in recent years by PET ligands such as ^{11}C-PiB (Klunk *et al.*, 2004) and ^{18}F-FDDNP, used for imaging β-amyloid deposition. Unlike PiB, it has been suggested that FDDNP also binds to neurofibrillary tangles (Agdeppa *et al.*, 2001), which may contribute to ^{18}F-FDDNP retention in the mesial temporal cortex where β-amyloid-specific tracers such as ^{11}C-PiB scarcely bind (Kepe *et al.*, 2006; Ng *et al.*, 2007; Pike *et al.*, 2007; Rowe *et al.*, 2007).

Okamura and colleagues (2005) screened over 2000 small molecules to develop novel radiotracers with high affinity and selectivity for tau pathology/neurofibrillary tangles. Consequently, they identified a series of novel quinoline and benzimidazole derivatives that bind neurofibrillary tangles and, to a lesser extent, β-amyloid plaques. Serial analysis of those compounds led to the design and synthesis of a novel imaging agent, ^{18}F-THK523. The purpose of this study was to utilize a series of *in vitro*, *ex vivo* and *in vivo* techniques to determine whether ^{18}F-THK523 satisfied a number of radioligand criteria, assessing its suitability for the quantitative imaging of tau pathology in the human brain.

Materials and methods

Materials

All reagents were purchased from Sigma, unless otherwise stated. Human β-amyloid$_{1-42}$ was purchased from the W. M. Keck Laboratory (Yale University).

Mice

Mice were housed in conditions of controlled temperature (22 ± 2°C) and lighting (14:10 h light–dark cycle) with free access to food and water. rTg(TauP301L)4510 and their wild-type (CamKII) littermates were a kind gift from Jada Lewis (Dept Neuroscience, Mayo Clinic, Florida, USA) and APP/PS1 [B6C3-Tg(APPswe, PSEN1dE9)85Dbo/J] and wild-type littermates were purchased from JAX® Mice and Services. MicroPET studies employed 6-month-old rTg(TauP301L)4510 mice and 12-month-old APP/PS1 [B6C3-Tg(APPswe, PSEN1dE9)85Dbo/J] mice and their respective wild-type littermates.

Tissue collection and characterization

Human brain tissue was collected at autopsy. The sourcing and preparation of the human brain tissue was conducted by the Victorian Brain Bank Network. Alzheimer's disease pathological diagnosis was made according to standard NIA-Reagan Institute criteria (1997).

Determination of age-matched control cases were subject to the above criteria. Three Alzheimer's disease and three healthy, age-matched control cases were examined in this study.

^{18}F-labelling of THK523

Unlabelled THK523 and 2-(4-aminophenyl)-6-(2-tosyloxyethoxy)quinoline (BF241; the precursor for ^{18}F-THK523) were custom synthesized by Tanabe R&D Service Co. and confirmed for purity by reverse phase high-performance liquid chromatography, 1D nuclear magnetic resonance and mass spectrometry. ^{18}F-THK523 (Fig. 1) was synthesized by nucleophilic substitution of the tosylate precursor (BF-241). Following a 10-min reaction at 110°C, the crude reaction was partially purified on an activated Sep-Pak tC18 cartridge before undergoing semi-preparative reverse phase high-pressure liquid chromatography purification. Standard tC18 Sep-Pak reformulation produced ^{18}F-THK523 in >95% radiochemical purity. The radiochemical yield was 24% (non-decay corrected) and at end of synthesis, the average specific activity was 100 GBq/μmol (2.7Ci/μmol).

Measurement of octanol/water partition coefficient

^{18}F-THK523 (37 MBq) was added to a mixture of 3 ml 1-octanol and 3 ml of 1 M potassium phosphate buffer (pH 7.4). The mixture was shaken for 30 min, followed by centrifugation for 3 min. Aliquots (0.5 ml) were carefully taken from each phase for assay. The partition coefficient was calculated as follows: (count per minute/0.5 ml l-octanol)/(count per minute/0.5 ml buffer). Measurements were done in triplicate.

Generation and protein purification of K18Δ280 K-tau

K18Δ280 K-tau is a fragment of the full length protein, htau40 (Barghorn *et al.*, 2004; von Bergen *et al.*, 2006) comprising the four repeat regions of tau including residues 243–372. Polymerase chain reaction was implemented to generate K18Δ 280 K-tau from plasmids kindly provided by the Mayo Clinic. Δ280K refers to the deletion of the lysine residue at position 280. DNA encoding this region was cloned into expression vector pET15b at the NcoI and XhoI sites and transfected into BL21DE3 *Escherichia coli*. Ampicillin selected *E. coli* were lysed in buffer comprising 50 mM PIPES pH 6.9, 1 mM EDTA, 5 mM dithiothreitol and protease inhibitor cocktail (Roche), sonicated on ice (6 × 30 min, with 30 s rest intervals) and the lysate was then spun at 18 000*g* at 4°C for 15 min. The supernatant was removed and added to a solution of NaCl at a final concentration of 0.5 M. The sample was then boiled for 20 min prior to centrifugation using the abovementioned conditions. The supernatant was then applied to a PD10 column (Amersham) and equilibrated in equilibration buffer (50 mM Tris pH 8.2, 20 mM NaCl, 1 mM EDTA, 5 mM dithiothreitol) and filtered prior addition to a SP sepharose column. Protein fractions were then analysed by Coomassie staining and western blot and appropriate fractions containing a single tau band were pooled, buffer exchanged into water (PD10), lyophilized and stored at −80°C.

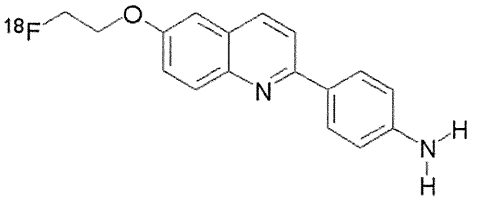

Figure 1 Chemical structure of ^{18}F-THK523 [2-(4-aminophenyl)-6-(2-fluoroethoxy)quinoline)].

Preparation of β-amyloid$_{1-42}$ and tau fibrils

Synthetic β-amyloid$_{1-42}$ was dissolved in 1 × phosphate buffered saline pH 7.7 to a final concentration of 200 μM. K18Δ280K-tau was dissolved in 1 × phosphate buffered saline pH 7.4 buffer to a final concentration of 20 μM. The solutions were then incubated at 37°C for 2 and 3 days, respectively, with agitation at 220 and 800 rpm, respectively (Orbital mixer incubator, Ratek). β-amyloid$_{1-42}$ fibril aggregation was confirmed via thioflavin T fluorescence spectroscopy and tau aggregation was confirmed by thioflavin S fluorescence spectroscopy; both fibril preparations were examined by transmission electron microscopy.

Thioflavin S/thioflavin T fluorescence

Aggregation of β-amyloid$_{1-42}$ fibril was confirmed using thioflavin T fluorescence (LeVine, 1999). Reactions (100 μl) comprising 20 μM β-amyloid$_{1-42}$ fibrils, 10 μM thioflavin T, 50 mM phosphate buffer were analysed at 444 nm (excitation) and 450–550 nm (emission), with an integration time of 1 s. K18Δ280K-tau fibril formation was confirmed by thioflavin S fluorescence whereby reactions comprising K18Δ280K-tau fibrils, 0.005% thioflavin S in 1 × phosphate buffered saline pH 7.4 were analysed at 440 nm (excitation) and 480 nm (emission), with an integration time of 1 s. Measurements were recorded using a Varian fluorescence spectrophotometer.

Transmission electron microscopy

Fibril formation of β-amyloid$_{1-42}$ and K18Δ280K-tau was further confirmed by transmission electron microscopy following staining with uranyl acetate. Carbon-coated copper electron microscopy grids were coated with K18Δ280K-tau or β-amyloid$_{1-42}$ fibrils, as described previously (Smith and Radford, 2001). Grids were viewed on a Siemens 102 transmission electron microscope, operating at a voltage of 60 kV.

In vitro ^{18}F-THK523 binding assays

Synthetic β-amyloid$_{1-42}$ or K18Δ280K-tau fibrils (200 nM) were incubated with increasing concentrations of ^{18}F-THK523 (1–500 nM). To account for non-specific binding of ^{18}F-THK523, the reactions described above were duplicated in the presence of unlabelled 1 μM THK523. The binding reactions were incubated for 1 h at room temperature in 200 μl of assay buffer [phosphate buffered saline, minus Mg^{2+} and Ca^{2+} (JRH Biosciences); 0.1% bovine serum albumin]. Separation of bound from free radioactivity was achieved by filtration under reduced pressure (MultiScreen HTS Vacuum Manifold; Multiscreen HTS 96-well filtration plates; 0.65 μm, Millipore). Filters were washed three times with 200 μl assay buffer and the radioactivity contained within the filters was counted in a γ-counter (Wallac 1480 Wizard 3"; Perkin Elmer). Binding data were analysed with curve fitting software that calculates the K_D and B_{max} using non-linear regression (GraphPad Prism Version 1.0, GraphPad Software). All experiments were conducted in triplicate.

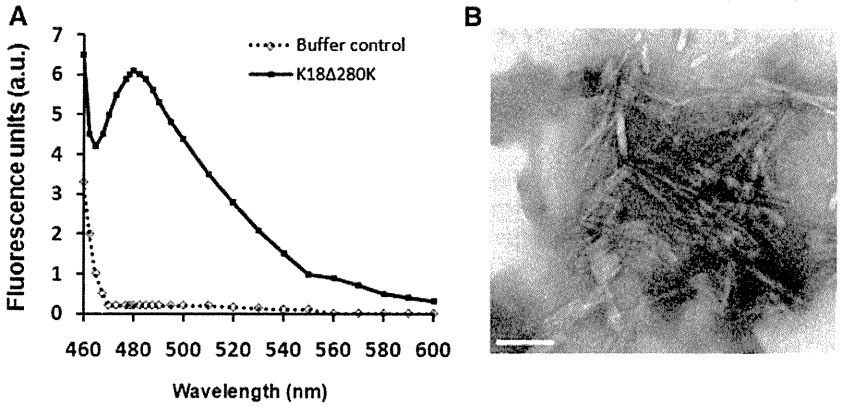

Figure 2 Characterization of K18Δ280K-tau fibrils. Recombinant K18(Δ280K)-tau was incubated with agitation (800 rpm) for 3 days at 37°C. **(A)** Graph depicting thioflavin S fluorescence, excitation/emission 440/480 nm, for K18Δ280K-tau (solid line) and no tau buffer control (dotted line). The graph for K18Δ280K-tau is indicative of positive amyloid fibril formation. **(B)** Electron microscopy image of K18Δ280K-tau fibrils. TechaniG^2 electron microscope; ×59 000 magnification. Scale bar: 50 nm. These data are representative of three independent experiments. a.u. = arbitrary units.

Immunohistochemistry and fluorescence analysis

Brain tissue from Alzheimer's disease and healthy control cases [three Alzheimer's disease (two female, one male), age range 75–83 years; three healthy controls (three female), age range 72–85 years], as well as mice (rTg4510, APP/PS1 and wild-type littermates) was fixed in 10% formalin/phosphate buffered saline and embedded in paraffin. For immunohistochemistry, 5 μm serial sections were deparaffinized and treated with 80% formic acid for 5 min and endogenous peroxidase activity was blocked with 3% hydrogen peroxide. Sections were then treated with blocking buffer (20% foetal calf serum, 50 mM Tris–HCl, 175 mM NaCl pH 7.4) before incubation with primary antibodies to β-amyloid (1E8; 1:50) or tau pAb (DAKO), for 1 h at room temperature. Serial 5 μm tissue sections were stained as follows: the first and third sections were immunostained with tau or 1E8 antibodies to identify tau tangles or β-amyloid plaques, respectively. The second serial section was stained with unlabelled THK523 to assess whether THK523 staining co-localized with the immunodetected tau tangles and/or β-amyloid plaques. Visualization of antibody reactivity was achieved with the LSAB™ kit (labelled streptavidin-biotin, DAKO) and sections were then incubated with hydrogen peroxidase-diaminobenzidine (H_2O_2-DAB) to visualize the tau tangles or β-amyloid-positive deposits. Sections were counterstained with Mayer's haematoxylin. To detect THK523 fluorescence, quenching was first performed whereby sections were first deparaffinized and tissue autofluorescence minimized by treatment of sections with 0.25% $KMnO_4$/phosphate buffered saline for 20 min prior to washing (phosphate buffered saline) and incubation with 1% potassium metabisulphite/1% oxalic acid/phosphate buffered saline for 5 min. Following autofluorescence quenching, sections were blocked in 2% bovine serum albumin/phosphate buffered saline pH 7.0 for 10 min and stained with 100 μM THK523 for 30 min. Washed (phosphate buffered saline) sections were then mounted in non-fluorescent mounting media (DAKO). Epifluorescence images were visualized on a Zeiss microscope [47CFP; filter set 47 (EM BP 436/20, BS FT 455, EM BP480/40)]. Co-localization of the THK523 and antibody signals was assessed by overlaying images from each of the stained serial tissue sections.

Autoradiography

For autoradiography, the hippocampal brain section of a patient with Alzheimer's disease (90-year-old female) was incubated with 2.2 MBq/ml of ^{18}F-THK523 at room temperature for 10 min and then washed briefly with water and 50% ethanol. After drying, the labelled section was exposed to a BAS-III imaging plate (Fuji Film) overnight. Autoradiographic images were obtained using a BAS-5000 phosphor imaging instrument (Fuji Film) with a spatial resolution of 25 × 25 μm. Neighbouring sections were immunostained using AT8 anti-tau monoclonal antibody (Innogenetics; diluted 1:20) or 6F/3D anti-Aβ antibody (DAKO; diluted 1:50).

Ex vivo biodistribution of ^{18}F-THK523

^{18}F-THK523 (0.68–1.32 MBq) was administered into the tail vein of ICR mice (n = 20, male, average weight 28–32 g). The mice were then sacrificed by decapitation at 2, 10, 30, 60 and 120 min post injection. The brain, blood and other organs were removed and weighed, and the radioactivity was counted with an automatic γ-counter. The percentage injected dose per gram (%ID/g) was calculated by comparison of tissue count to tissue weight. Each %ID/g value is an average ± SD of four separate experiments.

Small animal positron emission tomography imaging

All PET scans were conducted using a Philips MOSAIC small animal PET scanner with a transaxial spatial resolution of 2.7 mm full-width at half-maximum. Mice [n = 8 rTg4510 (four females, four males), n = 7 wild-type (four females, three males) mice and n = 3 APP/PS1 (all females) and three of their wild-type littermates (all females)] were intravenously injected with 100 μl of radiotracer comprising 3.7 MBq (0.35 μg/kg) of ^{18}F-THK523 via the tail vein. Mice were then anaesthetized using an isoflurane vaporizer with oxygen flow metre set to 5 l/min/5% isoflurane. Anaesthesia was maintained in a Veterinaire MINERVE anaesthetic assembly with the oxygen flow metre set to 2 l/min and vaporizer setting at 2%. A series of 6 × 5-min dynamic

emission scans were acquired starting at 5 min after injection. All images were reconstructed using a 3D row action maximum likelihood algorithm (RAMLA). Summed 25–35 min post-injection images were used for comparison between transgenic and wild-type mice. Image analysis was conducted using Wasabi v.2.0 software.

Statistical analysis

Normality of distribution was tested using the Shapiro–Wilk test and visual inspection of variable histograms. Statistical evaluations to assess differences in ^{18}F-THK523 binding were performed with analysis of variance (ANOVA) and a Tukey–Kramer Honestly Significant Difference test to establish differences between group means. Data are presented as mean ± SD unless otherwise stated.

Results

^{18}F-THK523 exhibits high affinity and selectivity for recombinant tau fibrils

To determine whether ^{18}F-THK523 satisfied the criteria of high affinity and selectivity for tau, the binding properties of ^{18}F-THK523 to tau fibrils was investigated and compared with β-amyloid$_{1–42}$ fibrils. A previously described truncated mutant of human tau, termed K18Δ280K-tau (Barghorn *et al.*, 2004; von Bergen *et al.*, 2006) that comprises the C-terminus of tau, including the four repeat regions and the FTDP-17 tau gene deletion resulting in the omission of lysine at position 280 (denoted Δ280K) was used for the studies. K18Δ280K-tau aggregates at low micromolar concentrations into paired helical filaments and straight filaments in the presence and absence of heparin (Perez *et al.*, 1996). Prior to conducting the binding assays, K18Δ280K-tau was formed into fibrillar structures (as monitored by thioflavin S fluorescence and transmission electron microscopy) by incubating 20 μM protein over 3 days at 37°C. On day 3, K18Δ280K-tau showed a thioflavin S fluorescence signal at ~480 nm (Fig. 2A), indicative of positive fibril formation. Fibril formation was confirmed by transmission electron microscopy with uranyl acetate staining (Fig. 2B). The β-amyloid$_{1–42}$ fibrils were generated as previously described (Fodero-Tavoletti *et al.*, 2007).

In vitro saturation studies were conducted using equimolar concentrations (200 nM, ~4.0×10^{-11} moles) of either K18Δ280-tau or β-amyloid$_{1–42}$ fibrils. While two classes of binding sites were identified on K18Δ280-tau fibrils (Fig. 3A) only one class of ^{18}F-THK523 binding sites was identified on β-amyloid$_{1–42}$ fibrils (Fig. 3B). Furthermore, there was a 10-fold higher affinity of ^{18}F-THK523 for the first class of K18Δ280-tau binding sites compared with β-amyloid$_{1–42}$ fibrils (Table 1). Overall, there was a ~5-fold higher number of ^{18}F-THK523 binding sites (B_{max}) on K18Δ280-tau fibrils, compared with β-amyloid$_{1–42}$ fibrils (Table 1).

THK523 demonstrates selectivity for tau pathology in sections of human hippocampal tissue

As a qualitative measure of its selectivity for tau pathology, THK523 recognition of tau pathology was assessed by histofluorescence and autoradiography. ^{19}F-THK523 and ^{18}F-THK523 share the same chemical structure, although ^{19}F is substituted for ^{18}F in the radiolabelled compound. For histofluorescence, unlabelled

Table 1 Binding parameters of ^{18}F-THK523 binding to fibrils

	K_{D1}	B_{max1}	K_{D2}	B_{max2}
K18Δ280K-tau fibrils	1.67	2.20	21.74	4.46
β-amyloid$_{1–42}$ fibrils	20.7	1.25		

K_D are in nM and B_{max} are in pmol ^{18}F-THK523/nmol fibrils.

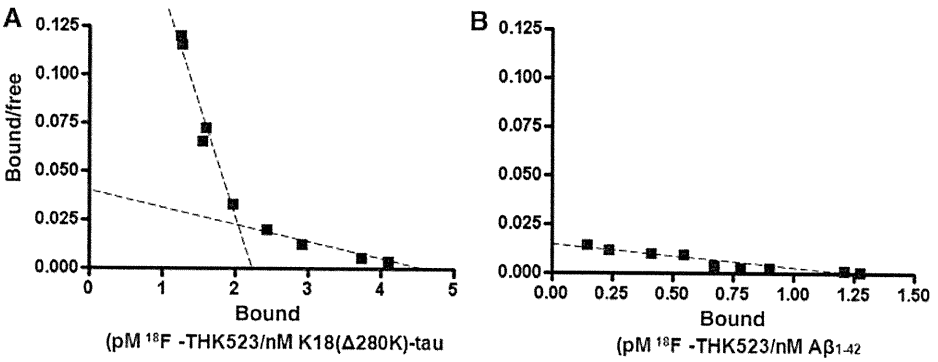

Figure 3 *In vitro* binding studies indicate two classes of ^{18}F-THK523-binding sites on K18Δ 280K-tau fibrils. Scatchard plots of ^{18}F-THK523 binding to synthetic K18Δ280K-tau (**A**) or (**B**) β-amyloid$_{1–42}$ fibrils. (**A**) Scatchard analysis identified two classes of THK523 binding sites on K18Δ280K-tau fibrils (K_{D1} and B_{max1} of 1.67 nM and 2.20 pmol THK523/nmol K18Δ280 K-tau, respectively; K_{D2} and B_{max2} of 21.7 nM and 4.46 pmol THK523/nmol K18Δ280 K-tau, respectively). (**B**) Scatchard analysis identified one class of THK523 binding sites on β-amyloid$_{1–42}$ with K_D and B_{max} of 20.7 nM and 1.25 pmol THK523/nmol β-amyloid$_{1–42}$. Binding data were analysed using GraphPad Software (Version 1.0). These data are the mean of three experiments for K18Δ280 K-tau and four experiments for β-amyloid fibrils.

THK523 binding to fixed serial sections from the hippocampus of subjects with Alzheimer's disease and age-matched controls was assessed. Contiguous sections were immunostained for β-amyloid and tau pathology with anti-β-amyloid and anti-tau antibodies, respectively. In all tissue sections examined, positive THK523 staining co-localized with tau pathology as detected in the contiguous tau immunostained section assessed (Fig. 4). THK523 failed to bind to diffuse β-amyloid plaques as indicated by the lack of co-localization with immunodetected β-amyloid pathology (Fig. 4). Likewise, autoradiography analysis in Alzheimer's disease hippocampal sections demonstrated that ^{18}F-THK523 bound to tau pathology with no ^{18}F-THK523 co-localization with immunodetected β-amyloid plaques (Fig. 5).

^{18}F-THK523 crosses the blood–brain barrier in mice

As well as being of low molecular weight (282.31 g/mol) and amenable to labelling with ^{18}F at high specific radioactivity [100 GBq/μmol (2.7 Ci/μmol)], a tau radiotracer should be adequately lipophilic to be able to cross the blood–brain barrier. The octanol/water coefficient ($logP_{oct}$) of ^{18}F-THK523 as a measure of lipophilicity, was calculated to be 2.91 ± 0.13. *Ex vivo* biodistribution studies of ^{18}F-THK523 in ICR mice, measured at 2, 10, 30, 60 and 120 min post injection, showed brain peak uptake of 2.75 ± 0.25% ID/g at 2 min post-intravenous injection (Fig. 6), indicating that ^{18}F-THK523 has adequate lipophilicity to cross the blood–brain barrier.

In vivo retention of ^{18}F-THK523 is significantly higher in tau transgenic mice brain compared with control and APP/PS1 mice

To further characterize ^{18}F-THK523 as a tau imaging radiotracer, *in vivo* microPET studies were performed to compare the retention of ^{18}F-THK523 in tau transgenic mice (rTg4510), versus their wild-type littermates (CamKII). Four independent studies were undertaken with 15 mice ($n = 8$ rTg4510 and $n = 7$ CamKII).

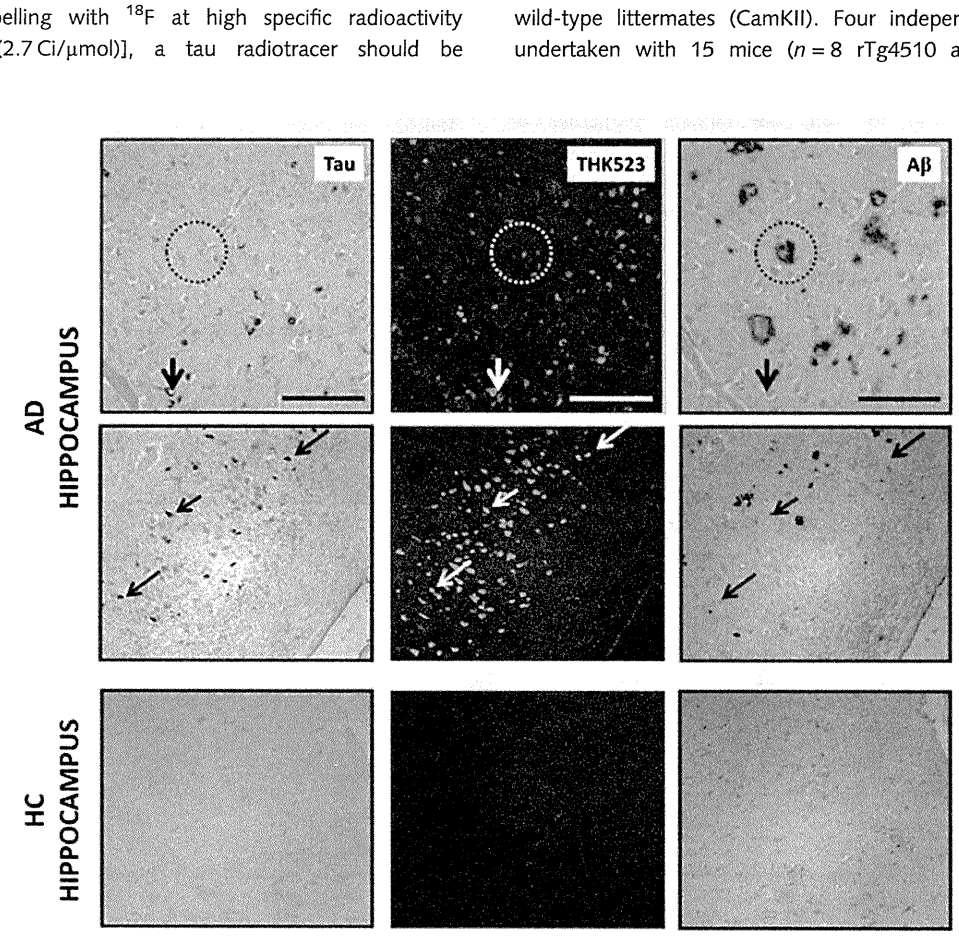

Figure 4 Histofluorescence analysis indicates that THK523 binds specifically to tau tangles with no detectable binding to β-amyloid plaques. Microscopy images of three serial sections (5 μm) from the hippocampus of a patient with Alzheimer's disease (AD) (*top* and *middle*) and a healthy control (HC) (*bottom*), immunostained with antibodies against tau (DAKO) and β-amyloid (1E8), to identify tau tangles and β-amyloid (Aβ) plaques, respectively; or stained with 100 μM THK523. Arrows indicate the location of tau tangles, while circles indicate the location of β-amyloid plaques. Positive THK523 staining appears to co-localize with tau immunostaining of neurofibrillary tangles in the hippocampus sections examined, but not to plaques. Tissue sections were imaged using a Zeiss microscope and Axiocam digital camera. Scale bars: 100 μm (*top*) and 200 μm (*middle* and *bottom*). These figures are representative of three subjects with Alzheimer's disease (two females, one male, age range 75–83 years) and three healthy controls (all female, age range 72–85 years).

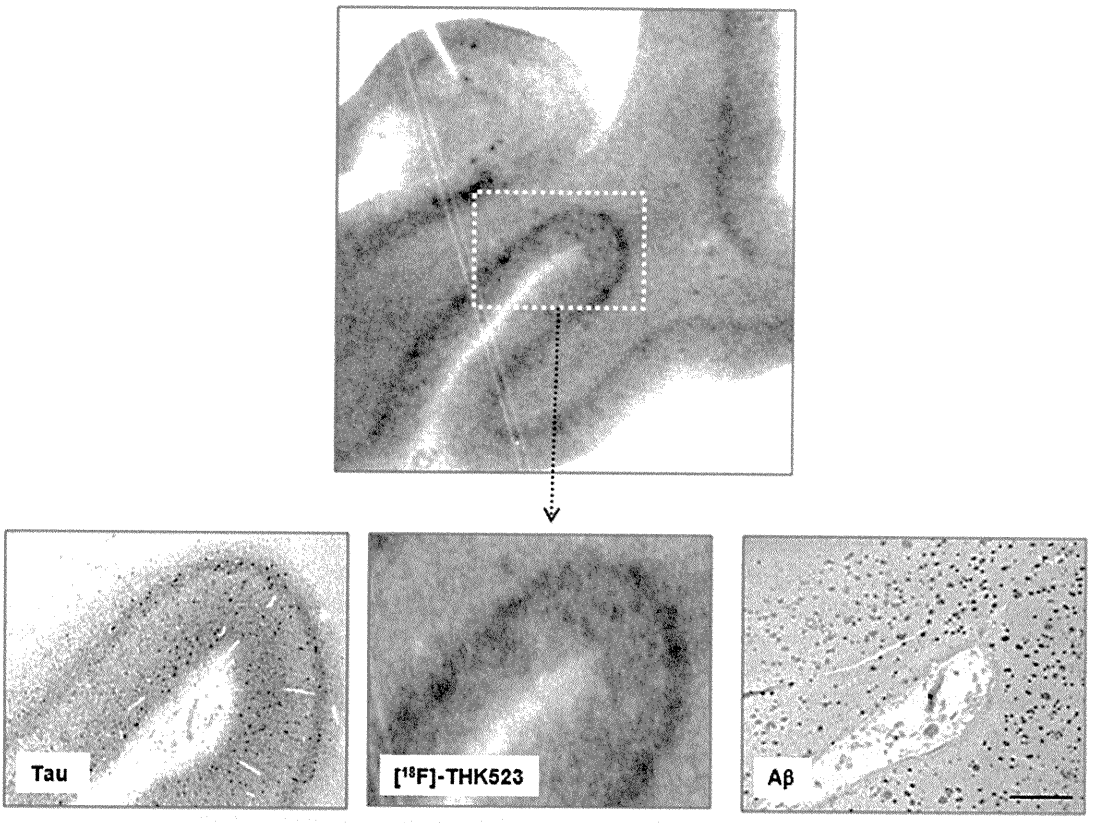

Figure 5 Autoradiography analysis indicates that ^{18}F-THK523 binds specifically to tau tangles with no detectable binding to β-amyloid plaques. (*Top*) ^{18}F-THK523 autoradiogram of Alzheimer's disease hippocampus (90-year-old female) serial section (low magnification). *Bottom*: microscopy images and autoradiogram (higher magnification) images of three serial sections (5 μm) from the hippocampus of the same Alzheimer's disease brain, immunostained with antibodies to tau (AT8, Innogenetics) and β-amyloid (6F/3D, DAKO), to identify tau tangles and β-amyloid (Aβ) plaques, respectively; or labelled with 2.2 MBq/ml ^{18}F-THK523. Positive ^{18}FTHK523 labelling appears to co-localize with tau immunostaining of neurofibrillary tangles in the hippocampus sections examined, but not to plaques. Scale bars: 500 μm. Autoradiographic images were obtained using a BAS-5000 phosphor imaging instrument (Fuji Film).

Representative microPET images are depicted in Fig. 7A and ^{18}F-THK523 time activity curves are depicted in Fig. 7C. Brain retention at ~30 min post injection of ^{18}F-THK523 was significantly higher (48%; $P < 0.007$) in the rTg4510 mice compared with their wild-type littermates (Fig. 7B). Analysis of bone, liver and intestine showed no significant differences in ^{18}F-THK523 retention (Fig. 7B), indicating a specific difference in brain uptake. Following microPET scanning, each mouse was euthanized and brains were harvested for biochemical and histofluorescence analysis. All rTg4510 mice brains examined were positive for tau overexpression as determined by western blot and immunohistochemical analysis (data not shown). Histofluorescence analysis of the same rTg4510 mice assessed by microPET identified positive THK523 staining that co-localized with immunopositive tau deposits (Fig. 8).

To further characterize the *in vivo* selectivity of ^{18}F-THK523 for tau pathology, microPET studies were conducted using the same experimental procedure in APP/PS1 transgenic mice ($n = 3$), exhibiting cerebral β-amyloid pathology but no tau deposits (Holcomb *et al.*, 1999). MicroPET analysis demonstrated that there was significantly lower retention of ^{18}F-THK523 in the brains of APP/PS1 mice, no different from the retention in their wild-type littermates ($n = 3$; Fig. 7B). Importantly, histofluorescence evaluation of rTg4510 and APP/PS1 brain tissue with 10 nM THK523 (a concentration that is achieved in the brain during PET studies), showed binding of THK523 to tau deposits in rTg4510 mice brains with negligible binding to β-amyloid plaques in the brain of APP/PS1 mice (Fig. 8).

Discussion

With the recent advances in instrumentation, image analysis and the development of new brain radiotracers, molecular neuroimaging with PET is rapidly expanding our knowledge base of neurodegenerative disease progression, improving early and accurate diagnosis, while promising to be effective in therapeutic monitoring and aiding in drug discovery and development. To date, much success has been achieved with β-amyloid radiotracers, in particular PiB being the best characterized radiotracer both *in vitro* and *in vivo*; showing selectivity for β-amyloid pathology resulting in a robust difference in ^{11}C-PiB brain retention in Alzheimer's disease

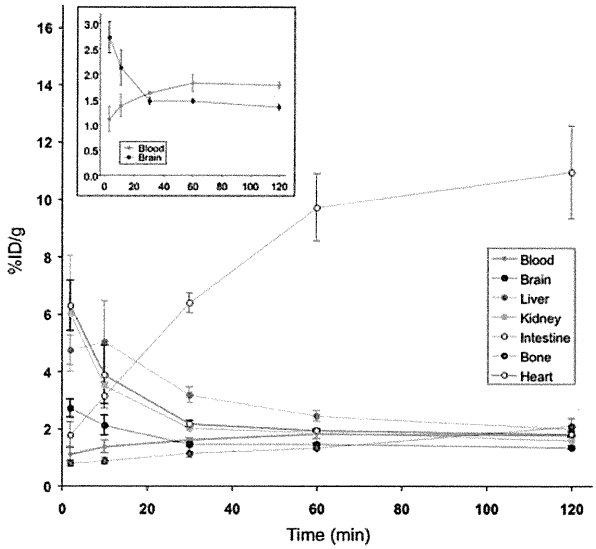

Figure 6 *Ex vivo* biodistribution studies of ^{18}F-THK523 in ICR mice. Initial uptake was highest (~6.2%ID/g) in the heart and kidney followed by a fast clearance. Liver radioactivity peaked (~5.0%ID/g) at 10 min after injection and was followed by a slow clearance, which mirrored a steady and substantial rise in radioactivity in the intestine (11%ID/g at 120 min after injection), suggesting that most of the tracer and/or its metabolites are eliminated through biliary excretion. There was a slow but steady increase in bone radioactivity, reaching a 2.1%ID/g at 120 min after injection, probably indicative of some degree of defluorination. The insert shows in better detail the brain and blood curves. Maximal ^{18}F-THK523 brain uptake (2.75%ID/g) was observed at 2 min after injection of the radiotracer, followed by a rapid clearance from the brain. Radioactivity in blood showed a different kinetic behaviour than the one observed in the brain, with a steady rise in radioactivity reaching an apparent plateau at about 60 min after injection. Uptake at each time point is expressed as percentage of injected dose per body weight (%ID/g) of ^{18}F-THK523. Curve represents the mean ± SD from four independent experiments. A total of 20 mice were examined.

compared with healthy aged-matched individuals in PET studies (Klunk *et al.*, 2004, 2005; Fodero-Tavoletti *et al.*, 2007, 2009). In addition to β-amyloid plaques, Alzheimer's disease brains are also pathologically characterized by the presence of tau pathology. Therefore, tau imaging may improve the specificity of diagnosis, allowing early detection of Alzheimer's disease and Pick's disease, where tau plays a role.

The identification and development of suitable PET radiotracer(s) is a demanding task especially given the considerable number of requirements that a radiotracer should fulfil to be deemed suitable for *in vivo* quantitative brain imaging. This study is the first to report a tau imaging radiotracer (^{18}F-THK523), that satisfies a number of criteria required for quantitative imaging of tau pathology in the human brain (Laruelle *et al.*, 2003; Nordberg, 2004; Pike, 2009). This study has shown that ^{18}F-THK523 has high affinity for recombinant tau fibrils and selectivity for tau fibrils/pathology over β-amyloid fibrils/pathology *in vitro*. Furthermore, it penetrates the blood–brain barrier, selectively highlighting tau pathology in the brains of rTg4510 tau transgenic mice *in vivo*.

In vitro saturation binding studies demonstrated that ^{18}F-THK523 binds to recombinant tau fibrils with high affinity in the low nanomole range. Typically ligands displaying affinities between 0.01–1.00 nM are deemed useful for *in vivo* quantitative PET studies. The high affinity ^{18}F-THK523-binding site (K_{D1}; 1.7 nM) exhibited >10-fold higher affinity compared with β-amyloid$_{1-42}$ fibrils (20.7 nM). Moreover, the number of high affinity ^{18}F-THK523-binding sites (K_{D1}) was almost 2-fold higher than the number of sites on β-amyloid$_{1-42}$ fibrils. In comparison to previous ^{3}H-PiB studies (Klunk *et al.*, 2005; Fodero-Tavoletti *et al.*, 2007), the affinity of ^{3}H-PiB for β-amyloid$_{1-42}$ (K_{D1}, 0.71–0.91 nM) is similar to the affinity of ^{18}F-THK523 for tau fibrils (K_{D1}, 1.7 nM). However, tau fibrils exhibit a larger number of ^{18}F-THK523 binding sites (B_{max1}, 2.20 pmol ^{18}F-THK523/nmol K18Δ280K-tau), compared with what has previously been reported for ^{3}H-PiB and β-amyloid$_{1-42}$ (1.01 pmol PiB/nmol β-amyloid$_{1-42}$) (Fodero-Tavoletti *et al.*, 2007). As the concentration of imaging radiotracers typically achieved during PET studies is in the low nanomole range, these findings strongly suggest that ^{18}F-THK523 will bind with high affinity and selectively to tau pathology under PET imaging conditions. Furthermore, as the brain area occupied by plaques is larger in comparison to neurofibrillary tangles, a >10-fold higher affinity and a larger number of ^{18}F-THK523-binding sites on tau/neurofibrillary tangles over β-amyloid plaques may prove essential in ascertaining a high tau signal over background in human PET studies (Laruelle *et al.*, 2003).

Further evidence of ^{18}F-THK523 selectivity for tau pathology was demonstrated by autoradiography and histofluorescence with positive THK523 staining, co-localizing with tau pathology and not with β-amyloid plaques in human Alzheimer's disease hippocampal sections. Importantly, even at THK523 concentrations 10 000-fold higher than those typically achieved under PET studies, THK523 failed to bind to diffuse plaques in the histofluorescence studies. There was some inconsistent staining of cored/compact plaques, suggesting that there might be some ^{18}F-THK523 binding to cored β-amyloid plaques, but only under non-PET radiotracer conditions. Similarly, variable staining of neurofibrillary tangles at high concentrations of PiB, has been reported by Ikonomovic and colleagues (2008).

In addition to high affinity and selectivity, a suitable tau radiotracer must be able to cross the blood–brain barrier to reach its target *in vivo*. The small size (molecular weight <450) (Laruelle *et al.*, 2003) and lipophilic nature of ^{18}F-THK523 [log P_{OCT} value of 2.9 ± 0.1; $-\log P_{OCT}$ values in the range of 0.9 and 3.0, show optimal entry into the brain (Dishino *et al.*, 1983)] indicates that ^{18}F-THK523 is able to penetrate the blood–brain barrier. This was confirmed in both *ex vivo* biodistribution and *in vivo* microPET imaging studies. Additionally, microPET imaging demonstrated that ^{18}F-THK523 retention was significantly higher (48%; $P = 0.007$) in the brains of rTg4510 tau transgenic mice compared with their control littermates, devoid of tau pathology; in agreement with the *in vitro* saturation and histofluorescence studies. Moreover, selectivity of THK523 for tau pathology was further supported by the ^{18}F-THK523 microPET assessment of APP/PS1 mice. These mice possess substantial cerebral β-amyloid plaque

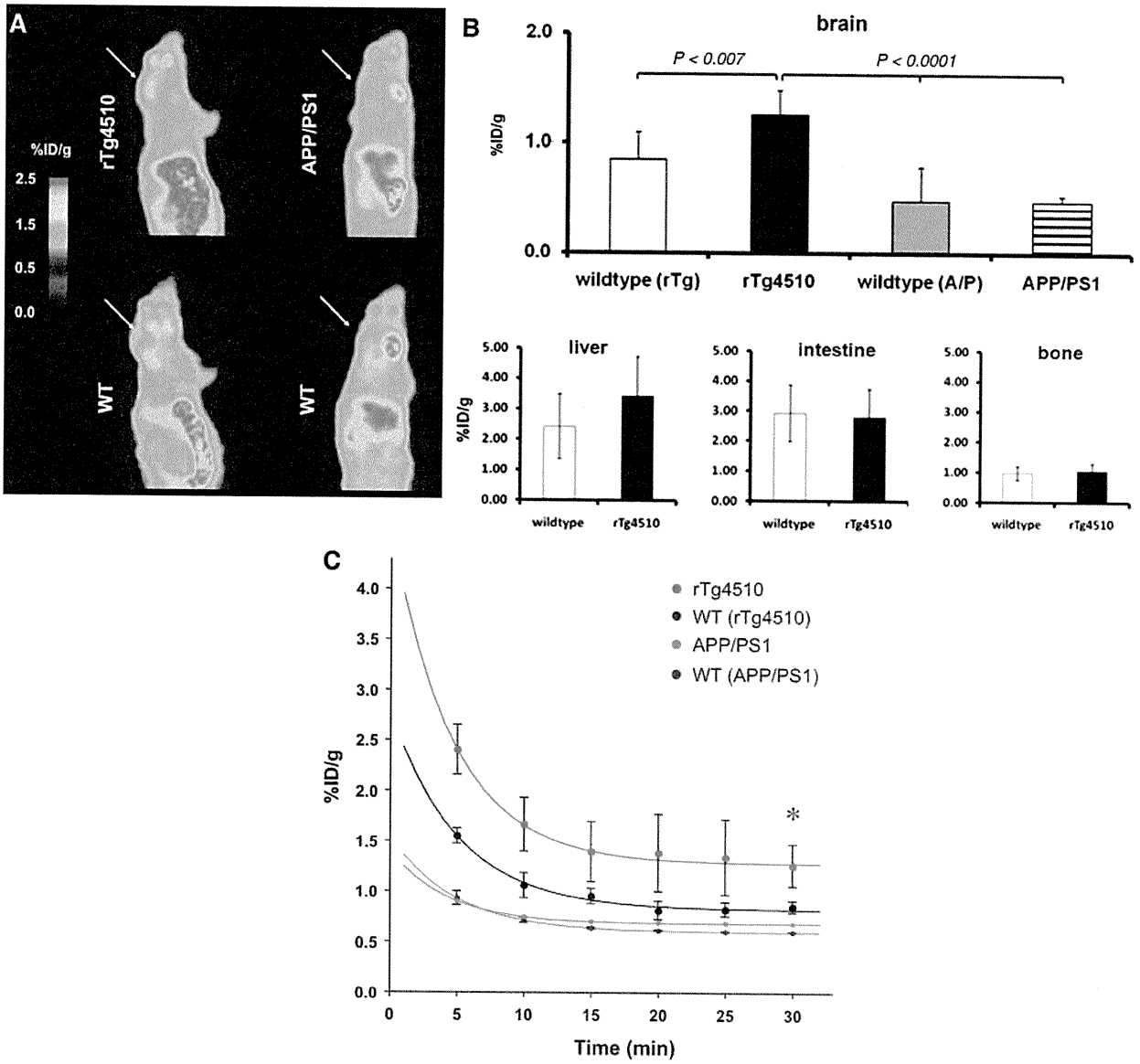

Figure 7 *In vivo* ^{18}F-THK523 microPET studies of tau and β-amyloid overexpressing transgenic mice. (**A**) Representative microPET scans at 30-min post injection of ^{18}F-THK523. rTg4510 mice (*top, left*) exhibited higher ^{18}F-THK523 brain retention compared with their wild-type (WT) littermate (*bottom, left*). Low ^{18}F-THK523 retention was observed APP/PS1 (*top, right*) versus their wild-type littermates (bottom, right). (**B**) Analysis of the ^{18}F-THK523 brain microPET data (30-min post injection) in rTg4510, APP/PS1 mice and their respective wild-type littermates revealed significantly higher (*) retention of ^{18}F-THK523 in the brain (*top*) of rTg4510 mice compared with APP/PS1 mice as well as their respective wild-type littermates. No significant differences in ^{18}F-THK523 retention were observed in the liver, intestine and bone (*bottom*). Data are presented as mean ± SD. (**C**) Brain time-activity curves of ^{18}F-THK523 microPET data expressed as percentage of injected dose per body weight (%ID/g) of ^{18}F-THK523 at each time point. Curve represents the mean ± SD of four independent studies employing $n = 8$ rTg4510 (four females, four males), $n = 7$ WT (four females, three males) mice and $n = 3$ APP/PS1 (all females) and three of the wild-type (all females) mice. Data are presented as mean ± SD.

load; however, the retention of ^{18}F-THK523 in these mice was significantly lower than in rTg4510 tau transgenic mice and not different from the retention in CamKII mice or their own wild-type littermates; suggesting that THK523 does not significantly bind to β-amyloid plaques and is selective for tau pathology *in vivo*.

Analysis of ^{18}F-THK523 biodistribution in the microPET studies showed no significant differences in ^{18}F-THK523 retention in the liver, intestine or bone between rTg4510 tau transgenic and wild-type mice. ^{18}F-THK523 retention in bone is indicative of some degree of defluorination (Van Dort *et al.*, 1995). *In vitro* stability testing showed that ^{18}F-THK523 was stable *in vitro*, suggesting that defluorination most likely occurs post-injection (data not shown). However, as the degree of free ^{18}F-bone retention is similar in both transgenic and control mice, the free ^{18}F does not

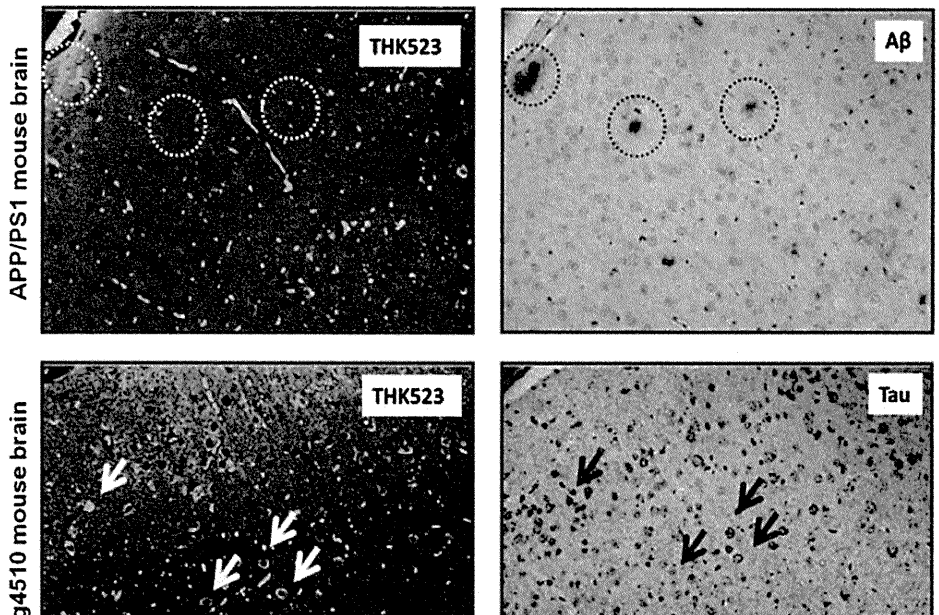

Figure 8 Co-localization of THK523 staining with tau pathology. Microscopy images of two serial sections (5 μm) from brains of rTg4510 and APP/PS1 mice immunostained with either tau (DAKO) or β-amyloid (1E8) antibodies, to identify tau tangles and β-amyloid (Aβ) plaques respectively; or stained with 10 nM THK523. Arrows indicate the location of tau tangles while circles indicate the location of β-amyloid plaques. Positive THK523 staining co-localize with tau immunostaining of neurofibrillary tangles, but not with β-amyloid plaques. Tissue sections were imaged with a Zeiss microscope and Axiocam digital camera. Scale bars: 100 μm. These data are representative of four independent studies employing eight rTg4510 and three APP/PS1 mice.

contribute differentially to the retention of ^{18}F-THK523 in the mouse brain. Similarly, as was observed in the *ex vivo* biodistribution studies, accumulation of radioactivity was observed within the intestine and liver of both rTg4510 and their control littermates indicating that most of the tracer and/or its metabolites were eliminated rapidly from the body through biliary excretion. Both tau transgenic and control littermates exhibited similar, low expression levels of tau in the liver (data not shown), further suggesting that ^{18}F-THK523 liver retention was due to the metabolic processing of ^{18}F-THK523 and not attributable to tau expression.

In conclusion, ^{18}F-THK523 is a novel tau radiotracer that fulfils the major criteria necessary for an 'ideal' PET radiotracer (Laruelle *et al.*, 2003; Nordberg, 2004). In addition to the abovementioned properties, THK523 was successfully labelled with ^{18}F with high specific activity. The relatively longer half-life of ^{18}F (110 min) precludes the need for an onsite cyclotron, allowing widespread distribution.

The clinical application of ^{18}F-THK523 as a selective tau imaging biomarker will provide important information regarding tau pathophysiology in Alzheimer's disease and non-Alzheimer's disease tauopathies, allowing correlation of brain tau load with cognitive function, monitoring disease progression and evaluation of therapeutic efficacy of newly developed drugs; especially aimed at modulating tau pathology (Gozes *et al.*, 2009; Hampel *et al.*, 2009*a*, *b*; Wischik and Staff, 2009). This study provides an important and critical step in defining the role of ^{18}F-THK523 as a tau specific PET radiotracer.

Acknowledgements

We thank Fairlie Hinton and Geoff Pavey from the Victorian Brain bank Network for sourcing and preparation of the human brain tissue.

Funding

National Health and Medical Research Council of Australia (in part); Neurosciences Victoria and the Ministry of Health, Labour and Welfare, Japan (in part); Industrial Technology Research Grant Program in 2009 from New Energy and Industrial Technology Development Organization (NEDO) of Japan(in part); AAR Viertel Fellowship (to M.T.F.-T.); NHMRC Senior Research Fellowship (to R.C. and K.J.B.). Perpetual Trustees H & L Hecht Trust.

References

Agdeppa ED, Kepe V, Liu J, Flores-Torres S, Satyamurthy N, Petric A, et al. Binding characteristics of radiofluorinated

6-dialkylamino-2-naphthylethylidene derivatives as positron emission tomography imaging probes for beta-amyloid plaques in Alzheimer's disease. J Neurosci 2001; 21: RC189.

Arriagada PV, Growdon JH, Hedley-Whyte ET, Hyman BT. Neurofibrillary tangles but not senile plaques parallel duration and severity of Alzheimer's disease. Neurology 1992; 42 (3 Pt 1): 631–9.

Barghorn S, Davies P, Mandelkow E. Tau paired helical filaments from Alzheimer's disease brain and assembled in vitro are based on beta-structure in the core domain. Biochemistry 2004; 43: 1694–703.

Blennow K, Hampel H. CSF markers for incipient Alzheimer's disease. Lancet Neurol 2003; 2: 605–13.

Cairns NJ, Ikonomovic MD, Benzinger T, Storandt M, Fagan AM, Shah A, et al. Absence of Pittsburgh compound B detection of cerebralamyloid beta in a patient with clinical, cognitive, and cerebrospinal fluidmarkers of Alzheimer disease. Arch Neurol 2009; 66: 1557–62.

Choi SR, Golding G, Zhuang Z, Zhang W, Lim N, Hefti F, et al. Preclinical properties of 18F-AV-45: a PET agent for Abeta plaques in the brain. J Nucl Med 2009; 50: 1887–94.

Delaere P, Duyckaerts C, Brion JP, Poulain V, Hauw JJ. Tau, paired helical filaments and amyloid in the neocortex: a morphometric study of 15 cases with graded intellectual status in aging and senile dementia of Alzheimer type. Acta neuropathologica 1989; 77: 645–53.

Delaere P, Duyckaerts C, Masters C, Beyreuther K, Piette F, Hauw JJ. Large amounts of neocortical beta A4 deposits without neuritic plaques nor tangles in a psychometrically assessed, non-demented person. Neurosci Lett 1990; 116: 87–93.

Dickson DW. Neuropathological diagnosis of Alzheimer's disease: a perspective from longitudinal clinicopathological studies. Neurobiology of aging 1997; 18 (Suppl 4): S21–6.

Dishino DD, Welch MJ, Kilbourn MR, Raichle ME. Relationship between lipophilicity and brain extraction of C-11-labeled radiopharmaceuticals. J Nucl Med 1983; 24: 1030–8.

Duyckaerts C, Brion JP, Hauw JJ, Flament-Durand J. Quantitative assessment of the density of neurofibrillary tangles and senile plaques in senile dementia of the Alzheimer type. Comparison of immunocytochemistry with a specific antibody and Bodian's protargol method. Acta neuropathologica 1987; 73: 167–70.

Duyckaerts C, Delaere P, Hauw JJ, Abbamondi-Pinto AL, Sorbi S, Allen I, et al. Rating of the lesions in senile dementia of the Alzheimer type: concordance between laboratories. A European multicenter study under the auspices of EURAGE. J Neurol Sci 1990; 97: 295–323.

Ferreira ST, Vieira MN, De Felice FG. Soluble protein oligomers as emerging toxins in Alzheimer's and other amyloid diseases. IUBMB Life 2007; 59: 332–45.

Fodero-Tavoletti MT, Rowe CC, McLean CA, Leone L, Li QX, Masters CL, et al. Characterization of PiB binding to white matter in Alzheimer disease and other dementias. J Nucl Med 2009; 50: 198–204.

Fodero-Tavoletti MT, Smith DP, McLean CA, Adlard PA, Barnham KJ, Foster LE, et al. In vitro characterization of Pittsburgh compound-B binding to Lewy bodies. J Neurosci 2007; 27: 10365–71.

Ganzer S, Arlt S, Schoder V, Buhmann C, Mandelkow EM, Finckh U, et al. CSF-tau, CSF-Abeta1-42, ApoE-genotype and clinical parameters in the diagnosis of Alzheimer's disease: combination of CSF-tau and MMSE yields highest sensitivity and specificity. J Neural Transm 2003; 110: 1149–60.

Gozes I, Stewart A, Morimoto B, Fox A, Sutherland K, Schmeche D. Addressing Alzheimer's disease tangles: from NAP to AL-108. Curr Alzheimer Res 2009; 6: 455–60.

Hampel H, Blennow K, Shaw LM, Hoessler YC, Zetterberg H, Trojanowski JQ. Total and phosphorylated tau protein as biological markers of Alzheimer's disease. Exp Gerontol 2009a; 45: 30–40.

Hampel H, Ewers M, Burger K, Annas P, Mortberg A, Bogstedt A, et al. Lithium trial in Alzheimer's disease: a randomized, single-blind, placebo-controlled, multicenter 10-week study. J Clin Psychiatry 2009b; 70: 922–31.

Ho GJ, Gregory EJ, Smirnova IV, Zoubine MN, Festoff BW. Cross-linking of beta-amyloid protein precursor catalyzed by tissue transglutaminase. FEBS Lett 1994; 349: 151–4.

Holcomb LA, Gordon MN, Jantzen P, Hsiao K, Duff K, Morgan D. Behavioral changes in transgenic mice expressing both amyloid precursor protein and presenilin-1 mutations: lack of association with amyloid deposits. Behav Genet 1999; 29: 177–85.

Ikonomovic MD, Klunk WE, Abrahamson EE, Mathis CA, Price JC, Tsopelas ND, et al. Post-mortem correlates of in vivo PiB-PET amyloid imaging in a typical case of Alzheimer's disease. Brain 2008; 131 (Pt 6): 1630–45.

Jack CR Jr, Knopman DS, Jagust WJ, Shaw LM, Aisen PS, Weiner MW, et al. Hypothetical model of dynamic biomarkers of the Alzheimer's pathological cascade. Lancet Neurol 2010; 9: 119–28.

Katzman R, Terry R, DeTeresa R, Brown T, Davies P, Fuld P, et al. Clinical, pathological, and neurochemical changes in dementia: a subgroup with preserved mental status and numerous neocortical plaques. Ann Neurol 1988; 23: 138–44.

Kepe V, Huang SC, Small GW, Satyamurthy N, Barrio JR. Visualizing pathology deposits in the living brain of patients with Alzheimer's disease. Methods Enzymol 2006; 412: 144–60.

Klunk WE, Engler H, Nordberg A, Wang Y, Blomqvist G, Holt DP, et al. Imaging brain amyloid in Alzheimer's disease with Pittsburgh Compound-B. Ann Neurol 2004; 55: 306–19.

Klunk WE, Lopresti BJ, Ikonomovic MD, Lefterov IM, Koldamova RP, Abrahamson EE, et al. Binding of the positron emission tomography tracer Pittsburgh compound-B reflects the amount of amyloid-beta in Alzheimer's disease brain but not in transgenic mouse brain. J Neurosci 2005; 25: 10598–606.

Lambert MP, Viola KL, Chromy BA, Chang L, Morgan TE, Yu J, et al. Vaccination with soluble Abeta oligomers generates toxicity-neutralizing antibodies. J Neurochem 2001; 79: 595–605.

Laruelle M, Slifstein M, Huang Y. Relationships between radiotracer properties and image quality in molecular imaging of the brain with positron emission tomography. Mol Imaging Biol 2003; 5: 363–75.

Lee VM, Goedert M, Trojanowski JQ. Neurodegenerative tauopathies. Annu Rev Neurosci 2001; 24: 1121–59.

LeVine H 3rd. Quantification of beta-sheet amyloid fibril structures with thioflavin T. Methods Enzymol 1999; 309: 274–84.

Maeda J, Ji B, Irie T, Tomiyama T, Maruyama M, Okauchi T, et al. Longitudinal, quantitative assessment of amyloid, neuroinflammation, and anti-amyloid treatment in a living mouse model of Alzheimer's disease enabled by positron emission tomography. J Neurosci 2007; 27: 10957–68.

Maezawa I, Hong HS, Liu R, Wu CY, Cheng RH, Kung MP, et al. Congo red and thioflavin-T analogs detect Abeta oligomers. J Neurochem 2008; 104: 457–68.

McLean CA, Cherny RA, Fraser FW, Fuller SJ, Smith MJ, Beyreuther K, et al. Soluble pool of Abeta amyloid as a determinant of severity of neurodegeneration in Alzheimer's disease. Annals Neurol 1999; 46: 860–6.

Ng S, Villemagne VL, Berlangieri S, Lee ST, Cherk M, Gong SJ, et al. Visual assessment versus quantitative assessment of 11C-PIB PET and 18F-FDG PET for detection of Alzheimer's disease. J Nucl Med 2007; 48: 547–52.

Nordberg A. PET imaging of amyloid in Alzheimer's disease. Lancet Neurol 2004; 3: 519–27.

Okamura N, Suemoto T, Furumoto S, Suzuki M, Shimadzu H, Akatsu H, et al. Quinoline and benzimidazole derivatives: candidate probes for in vivo imaging of tau pathology in Alzheimer's disease. J Neurosci 2005; 25: 10857–62.

Perez M, Valpuesta JM, Medina M, Montejo de Garcini E, Avila J. Polymerization of tau into filaments in the presence of heparin: the minimal sequence required for tau-tau interaction. J Neurochem 1996; 67: 1183–90.

Pike VW. PET radiotracers: crossing the blood-brain barrier and surviving metabolism. Trends Pharmacol Sci 2009; 30: 431–40.

Pike KE, Savage G, Villemagne VL, Ng S, Moss SA, Maruff P, et al. Beta-amyloid imaging and memory in non-demented individuals: evidence for preclinical Alzheimer's disease. Brain 2007; 130 (Pt 11): 2837–44.

Rowe CC, Ackerman U, Browne W, Mulligan R, Pike KL, O'Keefe G, et al. Imaging of amyloid beta in Alzheimer's disease with 18F-BAY94-9172, a novel PET tracer: proof of mechanism. Lancet Neurol 2008; 7: 129–35.

Rowe CC, Ng S, Ackermann U, Gong SJ, Pike K, Savage G, et al. Imaging beta-amyloid burden in aging and dementia. Neurology 2007; 68: 1718–25.

Shoghi-Jadid K, Small GW, Agdeppa ED, Kepe V, Ercoli LM, Siddarth P, et al. Localization of neurofibrillary tangles and beta-amyloid plaques in the brains of living patients with Alzheimer disease. Am J Geriatr Psychiatry 2002; 10: 24–35.

van der Zee J, Sleegers K, Van Broeckhoven C. Invited article: the Alzheimer disease-frontotemporal lobar degeneration spectrum. Neurology 2008; 71: 1191–7.

Van Dort ME, Jung YW, Sherman PS, Kilbourn MR, Wieland DM. Fluorine for hydroxy substitution in biogenic amines: asymmetric synthesis and biological evaluation of fluorine-18-labeled beta-fluorophenylalkylamines as model systems. J Med Chem 1995; 38: 810–5.

von Bergen M, Barghorn S, Jeganathan S, Mandelkow EM, Mandelkow E. Spectroscopic approaches to the conformation of tau protein in solution and in paired helical filaments. Neurodegener Dis 2006; 3: 197–206.

Walsh DM, Klyubin I, Fadeeva JV, Cullen WK, Anwyl R, Wolfe MS, et al. Naturally secreted oligomers of amyloid beta protein potently inhibit hippocampal long-term potentiation in vivo. Nature 2002; 416: 535–9.

Wenk GL. Neuropathologic changes in Alzheimer's disease. J Clin Psychiatry 2003; 64 (Suppl 9): 7–10.

Wischik C, Staff R. Challenges in the conduct of disease-modifying trials in Alzheimer's disease: practical experience from a phase 2 trial of Tau-aggregation inhibitor therapy. J Nutr Health Aging 2009; 13: 367–9.

Wisniewski HM, Bancher C, Barcikowska M, Wen GY, Currie J. Spectrum of morphological appearance of amyloid deposits in Alzheimer's disease. Acta Neuropathol 1989; 78: 337–47.

HUMAN PSYCHOPHARMACOLOGY
Hum. Psychopharmacol Clin Exp 2011; **26**: 133–139.
Published online 24 March 2011 in Wiley Online Library
(wileyonlinelibrary.com) **DOI**: 10.1002/hup.1184

Brain histamine H1 receptor occupancy of loratadine measured by positron emission topography: comparison of H1 receptor occupancy and proportional impairment ratio

Nobuo Kubo[1,5], Michio Senda[2], Yasunori Ohsumi[1], Setsu Sakamoto[2], Keiichi Matsumoto[2], Manabu Tashiro[3], Nobuyuki Okamura[4] and Kazuhiko Yanai[3,4]*

[1]*Department of Otolaryngology, Kansai Medical University, Osaka, Japan*
[2]*Division of Molecular Imaging, Institute of Biomedical Research and Innovation (IBRI), Kobe, Japan*
[3]*Cyclotron and Radioisotope Center, Tohoku University, Sendai, Miyagi, Japan*
[4]*Department of Pharmacology, Tohoku University School of Medicine, Sendai, Japan*
[5]*Department of Otolaryngology, Osaka Dental University, Osaka, Japan*

Aims We have evaluated the sedative properties of H1-antihistamines by using positron emission tomography (PET) and ^{11}C-doxepin. The purpose of the present study was to measure histamine H1 receptor occupancy (H1RO) of loratadine 10 mg in patients with allergic rhinitis and to compare this occupancy with that of *d*-chlorpheniramine 2 mg, a first-generation antihistamine. We also compared our PET findings with the proportional impairment ratio reported by McDonald *et al.*

Methods The H1RO of loratadine 10 mg and *d*-chlorpheniramine 2 mg were evaluated in human brains in a double-blind and crossover design using ^{11}C-doxepin PET. Eleven young male patients with allergic rhinitis were examined by PET following oral single administration of loratadine 10 mg and *d*-chlorpheniramine 2 mg.

Results Loratadine 10 mg occupied 11.7 ± 19.5% of histamine H1 receptors in the cortex, whereas *d*-chlorpheniramine 2 mg occupied 53.0 ± 33.2% in the same area, suggesting a non-sedating property of loratadine at a dose of 10 mg. The H1RO values of loratadine and *d*-chlorpheniramine as well as those of previous studies were found to be significantly proportional to the proportional impairment ratio ($r = 0.899$).

Conclusion Measurement of H1RO is a sensitive and absolute method to characterize the non-sedating property of drugs with H1 antagonistic activity. Copyright © 2011 John Wiley & Sons, Ltd.

KEY WORDS—H1-antihistamine; histamine H1 receptor occupancy; loratadine; positron emission tomography (PET); proportional impairment ratio; non-sedating

INTRODUCTION

Histamine H1 antagonists—antihistamines—are among the most widely used medications because they are prescribed for the relief of symptoms of common allergic diseases, such as seasonal pollinosis, perennial nasal allergy and chronic urticaria, which affect more than 10% of children and more than 20% of adolescents and adults worldwide. In Japan, cedar pollinosis, which affects approximately 20% of the Japanese population in the early spring season, has great impact on both quality of life and social activity. Classical first-generation antihistamines for treatment of seasonal and perennial allergies are known to have undesirable side effects, including sedation and impaired psychomotor performance. Patients taking sedating antihistamines for seasonal nasal allergy have experienced a decrease in verbal learning, decision-making ability and psychomotor speed. Cockburn *et al.* (1999) have estimated that loss of work productivity in patients taking sedating antihistamines is 13% higher than that in patients prescribed non-sedating antihistamines.

Inevitably, classical antihistamines are prescribed or purchased over-the-counter by individuals unaware of their undesirable side effects and involved in occupations that require a high level of attention, such as those operating complex industrial systems and those in the aviation and other forms of transportation. For these professionals, it is essential that the use of

* Correspondence to: K. Yanai, MD, PhD, Professor, Department of Pharmacology, Tohoku University School of Medicine, 2-1 Seiryo-machi, Aoba-ku, Sendai 980-8575, Japan. Tel: +81-22-717-8055; Fax: +81-22-717-8060. E-mail: yanai@med.tohoku.ac.jp

Received 20 October 2010
Accepted 28 January 2011

sedating antihistamines is not combined with performance of essential skills. This is especially important in the management of seasonal and perennial allergies where side effects-associated health disturbance is likely. Thus, when considering social requirements for antihistamines, safety, appropriate regimen and absence of drug interaction seem to have priority over efficacy and cost. Recently, a GA^{2}LEN position paper raised the issue of better consumer protection by recommending that first-generation H1-antihistamines be no longer available over-the-counter, especially that second-generation non-sedating H1-antihistamines with superior risk/benefit ratio are widely available at competitive prices (Church *et al.*, 2010).

Emergence of the so-called second-generation antihistamines has provided freedom from the sedative properties of conventional antihistamines and enabled safer use in patients with special occupations. The sedative properties of conventional antihistamines are due to their penetration through the blood–brain barrier (BBB) and occupation of brain histamine H1 receptors (H1R). Using positron emission tomography (PET), Okamura *et al.* (2000) demonstrated that impaired cognitive performance induced by *d*-chlorpheniramine is parallel to its occupation of human brain H1R. The sedative properties of clinically used antihistamines have also been evaluated using PET in human healthy volunteers (Yanai and Tashiro, 2007). In fact, PET studies are recommended by a consensus group (Consensus Group on New-Generation Antihistamines [CONGA]) as one of the objective methods to determine the sedative properties of new-generation antihistamines (Holgate *et al.*, 2003).

Using a crossover design with placebo and positive internal control, previous studies have determined the impairment index for each antihistamine (Shamsi and Hindmarch, 2000; McDonald *et al.*, 2008). Accordingly, proportional impairment ratio (PIR) enabled the sedative potential of an individual antihistamine to be identified relative to all other antihistamines, and thus allowed ranking of antihistamines with respect to their ability to cause impairment of cognitive and psychomotor functions. Findings from PIR and PET clearly demonstrate that there are distinct classes of antihistamines with respect to their ability to impair cognitive function and psychomotor performance.

In this study, we determined human brain histamine H1 receptor occupancy (H1RO) of loratadine (a second-generation antihistamine) 10 mg and *d*-chlorpheniramine (a first-generation antihistamine) 2 mg by using PET in patients with allergic rhinitis. To confirm the consistency of our findings with published impairment index for each antihistamine, we examined the relationship between H1RO values of loratadine 10 mg and *d*-chlorpheniramine 2 mg, as well as those of previous studies of H1-antihistamines and overall PIR values reported by McDonald *et al.* (2008).

MATERIALS AND METHODS

Subjects

The study protocol was approved by the ethics committees of the IBRI and Kansai Medical University, and all experiments were performed in accordance with the declaration of Helsinki.

Nineteen young male patients aged 20–29 years with moderate or severe chronic allergic rhinitis were recruited and provided with a clear description of the study. After giving their informed consent, the subjects were examined by rhinologists and were confirmed to fit the study criteria. Eleven subjects were able to complete the study. Inclusion criteria were as follows: (i) score 2 or higher in specific IgE antibody titer; (ii) experience being under antihistamine drug treatment but not being dependent on it; and (iii) normal liver function with $\geq$3 mg/ml albumin. Exclusion criteria were glaucoma, prostatic hypertrophy and presence of morphologic abnormality or organic disease in brain magnetic resonance imaging (MRI) acquired on the first visit. To allow for drug washout, the subjects were instructed to refrain from taking antihistamine drugs or other cold medicine that contains them for 1 week before PET scan. The subjects were also told not to take any alcoholic drink or any central nervous system drugs on the day before PET scan and not to take any tea or coffee on the day of PET scan. The study was performed during the off-season of pollen allergy.

Study design

We designed a placebo-controlled, three-way crossover study with double-blind and double-dummy design. Two antihistamine drugs, loratadine (Claritin™, 10 mg; Schering-Plough Corporation, Osaka, Japan) and *d*-chlorpheniramine maleate (Polaramine™, 2 mg; Schering-Plough Corporation, Osaka, Japan), were used for the study. A placebo drug (a non-absorbable intestinal medicine, Biofermin™; Biofermin Corporation, Kobe, Japan) was used for both baseline measurement and double-dummy design. The drugs were prepared using the same capsules so that they would look the same. Pharmacokinetics data showed that the time to peak plasma concentration was 90 min for loratadine and 60 min for *d*-chlorpheniramine. By considering a capsule dissolving time of 15 min, PET scan was designed to start at 105 or 75 min after the administration of loratadine or *d*-chlorpheniramine, respectively.

Positron emission tomography measurement

^{11}C-Doxepin was synthesized by ^{11}C-methylation of *N*-desmethyl-doxepin with ^{11}C-methyliodide. Its radiochemical purity was >95%, and its specific activity was >3.1 MBq/nmol. The amount of ^{11}C-doxepin injected to each subject was <289 ng/kg. ^{11}C-Doxepin preparation and quality control were approved by the radiopharmaceutical committee of the Institute of Biomedical Research and Innovation, Kobe, Japan.

Each subject underwent three PET scans (baseline, *d*-chlorpheniramine and loratadine) in a random order and in a double-blind and double-dummy design. For PET scans with antihistamines, the subject was orally given loratadine and placebo at 105 and 75 min, respectively, prior to ^{11}C-doxepin injection or *d*-chlorphenilamine and placebo at 75 and 105 min, respectively. For baseline condition, the subject was orally given placebo at 75 and 105 min prior to ^{11}C-doxepin injection.

For PET measurement, each subject was intravenously injected with 768.3 ± 42.3 MBq (705.4–898.1 MBq) of ^{11}C-doxepin. At 10 min post-injection, 5 ml of blood was taken from the contralateral antecubital vein to measure plasma radioactivity concentration. Brain radioactivity was measured for 20 min starting 70 min post ^{11}C-doxepin injection by using ECAT EXACT HR+ (Siemens Healthcare, Surrey, UK) PET camera in a 2D mode with attenuation correction using measured attenuation map acquired in the post-injection transmission scan. In each subject, subjective sleepiness was measured using the line analog rating scale after scanning. For each antihistamine, the measured subjective sleepiness was compared with that following placebo administration.

Positron emission tomography data analysis

All PET images, after being corrected for scattering and for tissue attenuation using post-injection transmission scan data, were reconstructed with a filtered back-projection algorithm. Standardized uptake values from a 15-min-long emission scan were calculated to yield static images reflecting distribution volume (DV). In our previous investigation, we have confirmed that ^{11}C-doxepin-H1Rs binding is better described with DV derived from a two-compartment model than with binding potential ratios (BPRs) derived from a three-compartment model (Mochizuki *et al.*, 2004a; Suzuki *et al.*, 2005). This allowed us to propose the use of DV as an index of quantitative measurement of H1Rs with ^{11}C-doxepin. We have also confirmed that DV of ^{11}C-doxepin-H1Rs binding could be stably reflected by plasma-radioactivity-normalized standardized uptake values from static 70- to 90 min images (Mochizuki *et al.*, 2004b), for which we adopted the static scan protocol in this study. Obviously, the simplified static scan protocol greatly reduces mental and physical stress of volunteers. In this study, we omitted normalization with plasma radioactivity data because we used relative DV values to those of cerebellum in each subject, which makes normalization with plasma radioactivity in the same individual unnecessary.

The three static DV images (after treatment with *d*-chlorpheniramine 2 mg, loratadine 10 mg or placebo) obtained from each subject were then co-registered using their T1-weighted MRIs and Statistical Parametric Mapping 2 software (SPM2) (Wellcome Department of Imaging Neuroscience, London, UK) (Friston *et al.*, 1995). Regions of interest (ROIs) were defined in the cortical regions, that is, frontal cortex, temporal cortex, parietal cortex, occipital cortex, thalamus and cerebellum, by placing three to five circles for each hemisphere in four to 10 consecutive brain transaxial slices. BPR in each ROI was calculated, and BPR images were created using the following equation: DV of each region/DV of cerebellum − 1. H1RO (as per cent of placebo baseline) was calculated in each ROI using the following equation: (1 − BPR of antihistamine/BPR of placebo) × 100% (Tashiro *et al.*, 2006; Yanai and Tashiro, 2007). BPR brain images were statistically analyzed on a voxel-by-voxel basis using SPM2, and regional maxima of statistical significance ($p < 0.005$) were projected onto surface-rendered MRI-T1 standard brain images. Precise locations of statistically significant regions were identified with the Co-planar Stereotaxic Atlas (Talairach and Tournoux, 1988).

Statistical analysis

Differences in H1RO between loratadine 10 mg and *d*-chlorpheniramine 2 mg were examined using Wilcoxon matched-pairs signed-ranks test, which was also used to examine for a significant difference in BPR between treatment conditions. The relationship between PIR values for all antihistamines included in the review and update paper of McDonald *et al.* (2008) and H1RO was examined using Pearson's correlation test. A probability of $p < 0.05$ was considered statistically significant.

RESULTS

^{11}C-Doxepin radioactivity distribution patterns were similar in the subjects treated with loratadine 10 mg or

placebo. That is, the radioligand apparently accumulated in H1R-rich cortical regions. However, in the subject treated with *d*-chlorpheniramine 2 mg, ^{11}C-doxepin radioactivity distribution appeared much lower than that in the subjects who received loratadine 10 mg or placebo. Using SPM2 on a voxel-by-voxel basis, parametric brain BPR images following treatment with *d*-chlorpheniramine 2 mg were statistically compared with those obtained following treatment with loratadine 10 mg. As shown in Figure 1A, brain regions with statistically lower BPRs of *d*-chlorpheniramine 2 mg than those obtained with loratadine 10 mg are indicated in red ($p < 0.005$). In the subjects treated with *d*-chlorpheniramine 2 mg, most brain regions demonstrated significantly lower BPRs than those of loratadine 10 mg-treated subjects. On the other hand, the difference in BPRs between the subjects treated with loratadine 10 mg and those treated with the placebo was negligible (Figure 1B).

Calculation of BPRs in the different ROIs revealed significantly lower values in the case of *d*-chlorpheniramine 2 mg than in the case of loratadine 10 mg or the placebo in cortical regions ($p < 0.05$), although no significant difference between lortadine 10 mg and the placebo was observed (Table 1).

Histamine H1 receptor occupancy following *d*-chlorpheniramine 2 mg or loratadine 10 mg treatment was also calculated using H1RO after placebo treatment as baseline (0%). H1RO following *d*-chlorpheniramine 2 mg treatment was significantly higher than that following loratadine 10 mg treatment in all cortical regions studied ($p < 0.05$, Table 2). Mean H1RO across all cortical regions following *d*-chlorpheniramine 2 mg treatment was approximately 53.0 ± 33.2% and that following loratadine 10 mg treatment was approximately 11.7 ± 19.5%. The difference between mean cortical H1RO following treatment with *d*-chlorpheniramine 2 mg and loratadine 10 mg was statistically significant ($p < 0.01$, Table 2). No statistical difference in sleepiness was demonstrated among the subjects treated with loratadine 10 mg or the placebo, although subjects treated with *d*-chlorpheniramine 2 mg showed significantly higher sleepiness scores than those treated with loratadine 10 mg or the placebo (data not shown).

Figure 2 shows values of H1RO for all antihistamines, including those used in this study. The correlation between PIR values for all antihistamines included in the review and update paper of McDonald *et al.* (2008) and H1RO is plotted in Figure 3. A significant correlation was observed between PIR and H1RO by Pearson's correlation test (PIR = 0.0344 × HIRO − 0.1456; correlation coefficient = 0.899; $p < 0.0005$).

DISCUSSION

It is well known that first-generation antihistamines often induce sedation as a side effect to their main anti-allergic action. Sedating antihistamines that easily penetrate the BBB occupy a large proportion of H1R, and variations in brain H1RO are due to different BBB

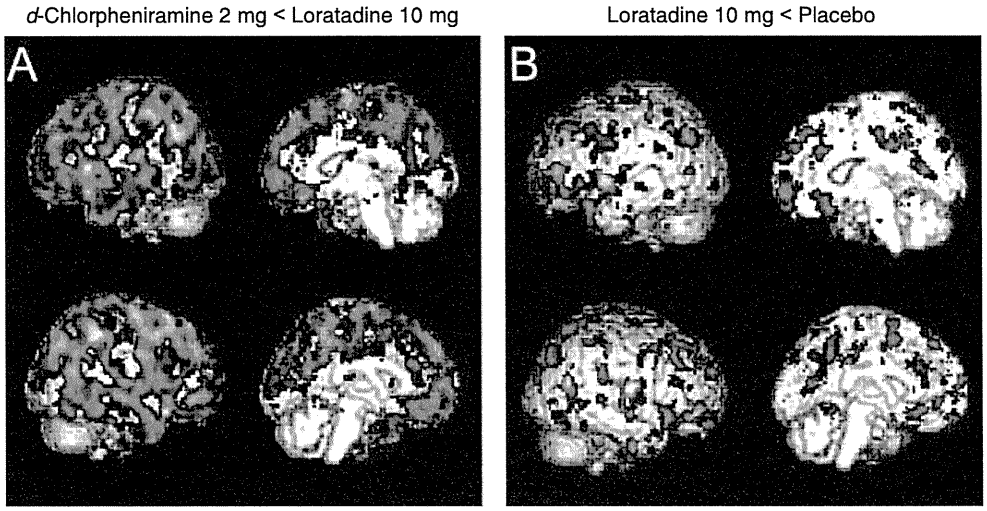

Figure 1. Results of voxel-by-voxel comparison between loratadine, *d*-chlorphenilamine and placebo. (A) Brain regions with statistically lower binding potential ratios (BPRs) of *d*-chlorpheniramine 2 mg than loratadine 10 mg are shown in red. Height threshold of voxel values was set at $p < 0.005$, and extent threshold was set at a 10-voxel minimum. Results were not corrected for multiple comparisons. Note that the majority of the cortical area in the subjects treated with *d*-chlorpheniramine 2 mg shows lower BPRs than in the subjects treated with loratadine 10 mg. (B) Brain regions with statistically lower BPRs of loratadine 10 mg than placebo are shown in red. Inter-treatment differences (loratadine 10 mg < placebo) between the subjects treated with loratadine and placebo are negligible

DOI: 10.1002/hup

Table 1. Binding potential (Bmax/Kd) of ^{11}C-doxepin among the three treatment conditions

	Loratadine 10 mg	Chlorpheniramine 2 mg	Placebo
Frontal	0.231 ± 0.085 NS	0.094 ± 0.129*	0.224 ± 0.111
Temporal	0.375 ± 0.151 NS	0.228 ± 0.194*	0.372 ± 0.116
Parietal	0.368 ± 0.108 NS	0.221 ± 0.166*	0.354 ± 0.125
Occipital	0.199 ± 0.103 NS	0.100 ± 0.142 NS	0.171 ± 0.065
Thalamus	0.292 ± 0.076 NS	0.330 ± 0.159 NS	0.324 ± 0.154

Mean ± SD ($n = 11$).
NS, no significant difference when compared with placebo.
*$p < 0.05$ when compared with placebo.

Table 2. Comparison of H1 receptor occupancy of loratadine and *d*-chlorpheniramine

	Loratadine 10 mg (%)	Chlorpheniramine 2 mg (%)
Frontal	10.8 ± 18.9*	70.7 ± 30.8
Temporal	11.7 ± 16.8*	45.9 ± 28.2
Parietal	10.1 ± 16.5*	40.1 ± 33.3
Occipital	14.1 ± 25.9*	55.2 ± 40.3
Thalamus	15.0 ± 18.0 NS	17.9 ± 18.7

Mean ± SD ($n = 11$).
NS, no significant difference when compared with *d*-chlorpheniramine.
*$p < 0.01$ when compared with *d*-chlorpheniramine.

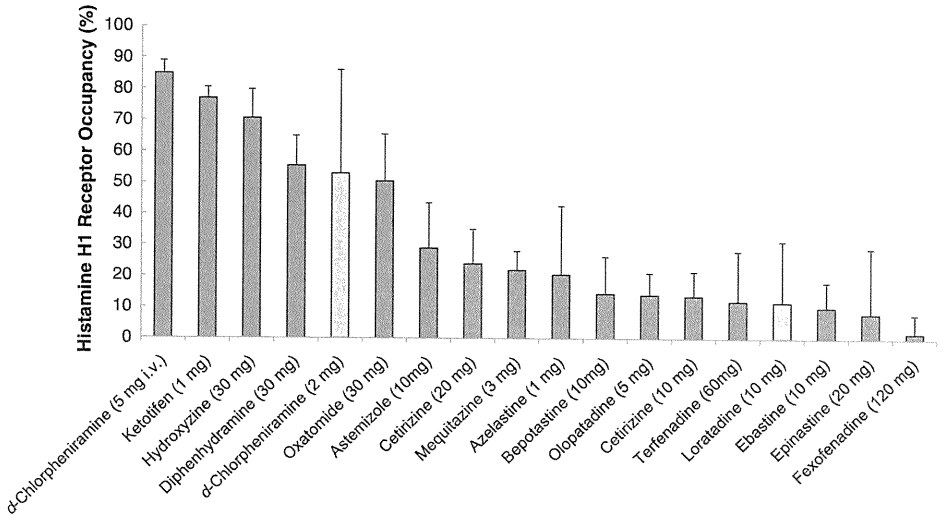

Figure 2. Histamine H1 receptor occupancy (H1RO) of various antihistamines. This figure summarizes H1RO values reported in the literature for various antihistamines. Values of H1RO of loratadine 10 mg and *d*-chlorpheniramine 2 mg are represented by the white columns

permeability. We have previously reported that H1RO can be measured using PET and ^{11}C-doxepin (Yanai *et al.*, 1995). This technique has over time proved to be a sensitive and absolute method for evaluating the sedative properties of antihistamines. Indeed, PET reveals that antihistamines that penetrate the BBB block H1R, whereas non-sedating antihistamines do not affect imaging patterns. In the present study, H1RO of loratadine 10 mg, a second-generation antihistamine, was compared with that of *d*-chlorpheniramine 2 mg, a typical sedating first-generation antihistamine. It is worthwhile noting here that H1RO of loratadine has not been determined in previous studies, although this drug is widely used worldwide (Boyle *et al.*, 2005). We found in this study that loratadine 10 mg occupies 11.7% of H1 receptor in the cortex of allergic patients, whereas *d*-chlorpheniramine 2 mg occupies 53.0% in the same area, indicating the non-sedating property of loratadine at a dose of 10 mg. Previous studies have also shown that *d*-chlorpheniramine 2 mg occupies 51% of H1 receptor in the cortex of healthy volunteers (Yanai and Tashiro, 2007). These findings suggest that there is no difference in H1RO of *d*-chlorpheniramine between healthy and allergic subjects.

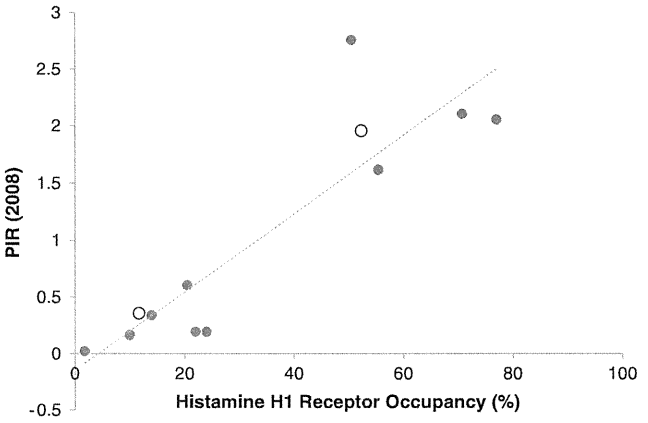

Figure 3. Correlation between proportional impairment ratio (PIR) (McDonald *et al.*, 2008) and histamine H1 receptor occupancy (H1RO) of various antihistamines. The H1RO values of this study as well as those of previous H1RO studies were compared with overall PIR values reported by McDonald *et al.* (2008) in order to confirm the consistency of our positron emission tomography findings with published impairment index for each antihistamine. Values of H1RO of loratadine 10 mg and *d*-chlorpheniramine 2 mg in this study are represented by white circles

Compared with previous PET studies on H1RO in healthy volunteers, this study provides clearer evidence of minimal H1RO by second-generation antihistamines, because it was performed in 11 patients with nasal allergy using a crossover double-blind and double dummy placebo-controlled protocol. Indeed, we found that brain H1RO of loratadine 10 mg is significantly less than that of *d*-chlorpheniramine 2 mg in patients with perennial nasal allergy. To the best of our knowledge, the present study is the first in allergic patients to verify the non-sedating properties of a worldwide second-generation antihistamine using a direct measure of central occupancy with PET.

Measurement of H1RO using PET seems to be a promising technique as recommended by the CONGA (Holgate *et al.*, 2003). CONGA states that all of the following three measurements should be undertaken to classify a specific antihistamine as non-sedating: (i) incidence of subjective sleepiness; (ii) objective cognitive and psychomotor functions; and (iii) PET measurement of H1RO. As impairment in objective performance has sometimes been observed in the absence of subjective sleepiness in a man following treatment with an antihistamine, the sedative properties of antihistamines should not be evaluated by subjective studies alone. Numerous studies have reported the results of various performance tests that compare the sedative profiles among antihistamines (Vuurman *et al.*, 1993; Weiler *et al.*, 2000; Tashiro *et al.*, 2005; Boyle *et al.*, 2006). However, because of limited sensitivity in psychomotor tests, it has sometimes been difficult to detect statistically significant differences when comparing two different second-generation antihistamines. PET studies on the other hand should provide a more objective and absolute method for evaluation of the sedative properties of antihistamines.

The findings of this study support those of clinical studies using subjective symptom score or neuropsychological task analysis to demonstrate the non-sedative and non-performance impairment of loratadine 10 mg (Kay and Harris, 1999). A meta-analysis of sedation and performance impairment of diphenhydramine versus second-generation antihistamines demonstrated that diphenhydramine significantly impaired performance relative to placebo or second-generation antihistamines, including loratadine (Bender *et al.*, 2003). These researchers, however, found that results of clinical studies varied and concluded that there was no clear consistent distinction between sedating and non-sedating antihistamines. Using PET in this study, we were able to demonstrate the non-sedating property of loratadine 10 mg. It is therefore clear that the non-sedating effect of new generation antihistamines should be evaluated by PET.

The histaminergic neuron system modulates wakefulness, the sleep–wake cycle, appetite control, learning, memory and emotion. In addition, it is known that neuronal histamine is important for stimulation and maintenance of wakefulness (Haas *et al.*, 2008; Watanabe and Yanai, 2001). First-generation antihistamines are known to occupy more than 50% of H1R and cause considerable sedation in man. More than 50% of H1RO is associated with high prevalence of sleepiness and cognitive impairment (Okamura *et al.*, 2000). As shown in Figure 2, antihistamines significantly vary in their H1RO. Antihistamines that occupy less than 10% of H1R are unlikely to cause impaired performances in cognitive tasks (Tashiro *et al.*, 2004, 2008, 2009). Based on these findings, the sedative properties of antihistamines can be divided into three categories: sedating, less-sedating and non-sedating (Yanai and Tashiro, 2007).

In the reviewed literature, Shamsi and Hindmarch (2000) and McDonald *et al.* (2008) have investigated the sedative potential of antihistamines for which data from objective and subjective psychometric assessments were available from double-blind, crossover studies assessing the effects of antihistamines on cognitive and psychomotor function in healthy volunteers. The findings of this investigation enabled the calculation of PIR for each drug under review, that is, the greater the PIR, the greater the cognitive and psychomotor impairment. In order to verify PIR and H1RO as

DOI: 10.1002/hup

measures of the sedative effect of antihistamines, we directly compared the values of PIR and H1RO and demonstrated a significant linear correlation between them as shown in Figure 3. This finding indicates that it is possible to differentiate between antihistamines using PIR and H1RO with respect to their potential to interfere with aspects of cognitive and psychomotor function and their potential to produce sedation. These considerations should be used by physicians to guide their decision in prescribing antihistamines.

In conclusion, we examined H1RO of loratadine 10 mg and compared it with that of *d*-chlorpheniramine 2 mg. Loratadine 10 mg occupied approximately 11% of available H1Rs in the cortex, confirming its non-sedating property at a dose of 10 mg. Judging from the positive correlation between PIR in published references and H1RO determined by PET, both PIR and H1RO can be used to evaluate the sedative property of antihistamines in humans. In particular, the direct comparison in H1RO among fexofenadine, desloratadine and levocetirizine would be interesting because the three second-generation antihistamines showing the PIR value of zero are most often prescribed as non-sedating antihistamines all over the world.

ACKNOWLEDGEMENTS

Decisions related to all aspects of the study, including design, conduct, and report, were made by study groups from multi-clinical trial centers in Japan.

CONFLICT OF INTEREST

This study was supported by Grant-in Aid for Scientific Research from the Ministry of Education, Science, Sports, and Culture of Japan (M. S., M. T., and K. Y.) and in part by Shionogi and Schering-Plough (providers of loratadine in Japan) as unrestricted grants (N. K., M. S.).

REFERENCES

Bender BG, Berning S, Dudden R, Milgrom H, Tran ZV. 2003. Sedation and performance impairment of diphenhydramine and second-generation antihistamines: a meta-analysis. *J Allergy Clin Immunol* **111**: 770–776.

Boyle J, Ridout F, Meadows R, Johnsen S, Hindmarch I. 2005. Suppression of the histamine-induced wheal and flare response by fexofenadine HCl 60 mg twice daily, loratadine 10 mg once daily and placebo in healthy Japanese volunteers. *Curr Med Res Opin* **21**: 1495–1503.

Boyle J, Eriksson M, Stanley N, Fujita T, Kumagi Y. 2006. Allergy medication in Japanese volunteers: treatment effect of single doses on nocturnal sleep architecture and next day residual effects. *Curr Med Res Opin* **22**: 1343–1351.

Church MK, Maurer M, Simons FER, *et al.* 2010. Risk of first-generation H1-antihistamines: a GA^{2}LEN position paper. *Allergy* **65**: 459–466.

Cockburn IM, Bailit HL, Berndt ER, Finkelstein SN. 1999. Loss of work productivity due to illness and medical treatment. *J Occup Environ Med* **41**: 948–953.

Friston KJ, Holmes AP, Worsley KJ, Poline JP, Frith CD, Frackowiak RS. 1995. Statistical parametric maps in functional imaging: A general linear approach. *Hum Brain Mapp* **2**: 189–210.

Haas HL, Sergeeva OA, Selbach O. 2008. Histamine in the nervous system. *Physiol Rev* **88**: 1183–1241.

Holgate ST, Canonica GW, Simons FE, *et al.* 2003. Consensus Group on New-Generation Antihistamines (CONGA): present status and recommendations. *Clin Exp Allergy* **33**: 1305–1324.

Kay GG, Harris AG. 1999. Loratadine: a non-sedating antihistamine. Review of its effects on cognition, psychomotor performance, mood and sedation. *Clin Exp Allergy* **29**(Suppl 3): 147–150.

McDonald K, Trick L, Boyle J. 2008. Sedation and antihistamines: an update. Review of inter-drug differences using proportional impairment ratios. *Hum Psychopharmacol* **23**: 555–570.

Mochizuki H, Kimura Y, Ishii K, *et al.* 2004a. Quantitative measurement of histamine H1 receptors in human brains by PET and [^{11}C]doxepin. *Nucl Med Biol* **31**: 165–171.

Mochizuki H, Kimura Y, Ishii K, *et al.* 2004b. Simplified PET measurement for evaluating histamine H1 receptors in human brains using [^{11}C]doxepin. *Nucl Med Biol* **31**: 1005–1011.

Okamura N, Yanai K, Higuchi M, *et al.* 2000. Functional neuroimaging of cognition impaired by a classical antihistamine, *d*-chlorpheniramine. *Br J Pharmacol* **129**: 115–123.

Shamsi Z, Hindmarch I. 2000. Sedation and antihistamines: a review of inter-drug differences using proportional impairment ratios. *Hum Psychopharmacol* **15**(S1): S3–S30.

Suzuki A, Tashiro M, Kimura Y, *et al.* 2005. Use of reference tissue models for quantification of histamine H1 receptors in human brain by using positron emission tomography and [11C] doxepin. *Ann Nucl Med* **19**: 425–433.

Talairach J, Tournoux P. 1988. *Co-planar stereotaxic atlas of the human brain.* Georg Thieme Verlag: Stuttgart, Germany.

Tashiro M, Sakurada Y, Iwabuchi K, *et al.* 2004. Central effects of fexofenadine and cetirizine: measurement of psychomotor performance, subjective sleepiness, and brain histamine H_1-receptor occupancy using ^{11}C-doxepin positron emission tomography. *J Clin Pharmacol* **44**: 890–900.

Tashiro M, Horikawa E, Mochizuki H, *et al.* 2005. Effects of fexofenadine and hydroxyzine on brake reaction time during car-driving with cellular phone use. *Hum Psychopharmacol* **20**: 501–509.

Tashiro M, Mochizuki H, Sakurada Y, *et al.* 2006. Brain histamine H1 receptor occupancy of orally administered antihistamines measured by positron emission tomography with 11C-doxepin in a placebo-controlled crossover study design in healthy subjects: a comparison of olopatadine and ketotifen. *Br J Clin Pharmacol* **61**: 16–26.

Tashiro M, Duan X, Kato M, *et al.* 2008. Brain histamine H1 receptor occupancy of orally administered antihistamines, bepotastine and diphenhydramine, measured by PET with ^{11}C-doxepin. *Br J Clin Pharmacol* **65**: 811–821.

Tashiro M, Kato M, Miyake M, *et al.* 2009. Dose dependency of brain histamine H1 receptor occupancy following oral administration of cetirizine hydrochloride measured using PET with [^{11}C]doxepin. *Hum Psychopharmacol* **24**: 540–548.

Vuurman EF, van Veggel LM, Uiterwijk MM, Leutner D, O'Hanlon JF. 1993. Seasonal allergic rhinitis and antihistamine effects on children's learning. *Ann Allergy* **71**: 121–126.

Watanabe T, Yanai K. 2001. Studies on functional roles of the histaminergic neuron system by using pharmacological agents, knockout mice and positron emission tomography. *Tohoku J Exp Med* **195**: 197–217.

Weiler JM, Bloomfield JR, Woodworth GG, *et al.* 2000. Effects of fexofenadine, diphenhydramine, and alcohol on driving performance. A randomized, placebo-controlled trial in the Iowa driving simulator. *Ann Intern Med* **132**: 354–363.

Yanai K, Tashiro M. 2007. The physiological and pathophysiological roles of neuronal histamine: an insight from human positron emission tomography studies. *Pharmacol Ther* **113**: 1–15.

Yanai K, Ryu JH, Watanabe T, *et al.* 1995. Histamine H1 receptor occupancy in human brains after single oral doses of histamine H1 antagonists measured by positron emission tomography. *Br J Pharmacol* **116**: 1649–1655.

Carbohydrate Polymers 87 (2012) 2237–2245

Contents lists available at SciVerse ScienceDirect

Carbohydrate Polymers

journal homepage: www.elsevier.com/locate/carbpol

Comb-shaped graft copolymers with cellulose side-chains prepared *via* click chemistry

Yukiko Enomoto-Rogers, Hiroshi Kamitakahara*, Arata Yoshinaga, Toshiyuki Takano

Division of Forest and Biomaterials Science, Graduate School of Agriculture, Kyoto University, Kitashirakawa-Oiwake-cho, Sakyo-ku, Kyoto 606-8502, Japan

ARTICLE INFO

Article history:
Received 3 September 2011
Received in revised form 20 October 2011
Accepted 20 October 2011
Available online 28 October 2011

Keywords:
Cellulose
Reducing-end
Comb-shaped graft copolymer
Cellulose side-chain
Click-chemistry

ABSTRACT

Comb-shaped copolymers with cellobiose acetate or cellulose triacetate (CTA) side-chains, PPMA-*g*-(CTA2-C15) and PPMA-*g*-(CTA13-C15), were prepared by grafting *N*-(15-azidopentadecanoyl)-2,3,6-tri-*O*-acetyl-4-*O*-(2,3,4,6-tetra-*O*-acetyl-β-D-glucopyranosyl)-β-D-glucopyranosylamine (CTA2-C15-N_3) and *N*-(15-azidopentadecanoyl)-tri-*O*-acetyl-β-cellulosylamine (CTA13-C15-N_3, number average degree of polymerization (DP_n) = 13) onto poly(2-propyn-1-yl methacrylate) (PPMA, weight average degree of polymerization (DP_w, $X+Y=5.59\times10^2$)) *via* "click chemistry". The copolymers were characterized by ^1H, ^{13}C and two-dimensional NMR and size exclusion chromatography–multi-angle laser light scattering (SEC–MALS) measurements. The numbers of CTA side-chains (X) of PPMA-*g*-(CTA2-C15) and PPMA-*g*-(CTA13-C15) were calculated as 4.03×10^2 and 2.45×10^2, respectively. Copolymers with cellulosic side-chains, PPMA-*g*-(CELL2-C15) and PPMA-*g*-(CELL13-C15), were successfully obtained after deacetylation of PPMA-*g*-(CTA2-C15) and PPMA-*g*-(CTA13-C15), respectively. X-ray diffraction measurements revealed that PPMA-*g*-(CELL13-C15) showed crystalline pattern of cellulose II, which is believed to have anti-parallel orientation.

1. Introduction

Cellulose is a linear (1→4)-β-glucopyranan having three hydroxyl groups per anhydroglucose unit. There have been several studies on cellulose graft copolymers, and a variety of polymers have been grafted onto the cellulose main-chain through its hydroxyl groups at C2, C3, and C6 positions to alter properties of cellulose or cellulosic materials (Dou & Jiang, 2007; Kang et al., 2006; Nishio, 2006). On the other hand, there have been many reports on glycopolymers with mono-, di-, or oligo-saccharides as pendent groups binding at the reducing-end on a main-chain (Kamitakahara et al., 1998; Ladmiral et al., 2006; Narumi, Miura, et al., 2006; Narumi, Otsuka, et al., 2006; Ohno, Fukuda, & Kitano, 1998; Ohno, Tsujii, & Fukuda, 1998). However, to our knowledge, there has been no report on a graft copolymer having cellulose side-chains. A comb-shaped copolymer with cellulose side-chains could achieve parallel orientation of cellulose molecules, and might have unique unknown properties such as crystallinity.

We have therefore prepared a novel graft copolymer with cellulose side-chains *via* free radical copolymerization of a cellulose macromonomer with methyl methacrylate, based on "graft through" (homo- or co-polymerization of macromonomers) strategy (Enomoto-Rogers, Kamitakahara, Nakayama, Takano, & Nakatsubo, 2009; Enomoto-Rogers, Kamitakahara, Takano, & Nakatsubo, 2009). The number of cellulose graft chains per main-chain was, however, only 3.86, because of low reactivity of a cellulose macromonomer, while the weight average degree of polymerization of poly(methyl methacrylate) main-chain was 4.14×10^2. It has been reported that the semi-flexible or rigid macromonomers such as methacrylate-end capped poly(n-hexyl isocyanate) (Kawaguchi, Mihara, Kikuchi, Lien, & Nagai, 2007; Se & Aoyama, 2004) are hard to polymerize, whereas other flexible macromonomers such as poly(ethylene oxide) (Ito, Tomi, & Kawaguchi, 1992) or poly(dimethylsiloxane) (Shinoda, Miller, & Matyjaszewski, 2001) are not.

On the other hand, "grafting onto" (attachment of side-chains to the backbone) strategy is known as another way to synthesize graft copolymers (Hourdet, L'Alloret, & Audebert, 1997; Kamitakahara et al., 1998; Poe, Jarrett, Scales, & McCormick, 2004). Thus, the "grafting onto" strategy was investigated to introduce more cellulose molecules as side-chains compared to our former study, and to control the orientation of cellulose chains.

Recently, the concept of "click chemistry" invented by Sharpless and coworkers (Kolb, Finn, & Sharpless, 2001; Wu et al., 2004) has been introduced into the synthesis of polymeric materials with well-defined and complex chain architectures. Specifically, Cu(I)-catalyzed Huisgen 1,3-dipolar cycloaddition between organic azides and terminal alkynes for the transformation of 1,2,3-triazoles has been received much attention as a highly efficient

* Corresponding author. Tel.: +81 75 753 6255; fax: +81 75 753 6300.
E-mail address: hkamitan@kais.kyoto-u.ac.jp (H. Kamitakahara).

0144-8617/$ – see front matter © 2011 Elsevier Ltd. All rights reserved.
doi:10.1016/j.carbpol.2011.10.055

and stereoselective reaction coupled with an excellent compatibility for functional groups. Ladmiral et al. (2006) have reported the preparation of glycopolymers by attaching azide containing mono-saccharides onto the alkyne containing polymer main-chain *via* "click chemistry".

In the present study, based on "grafting onto" strategy and "click chemistry", we prepared comb-shaped copolymers with cellulose side-chains, by grafting cellulose derivatives carrying a single azide group onto the alkyne containing polymer main-chain. Chemical structures of the synthesized graft copolymers and their crystalline patterns were investigated.

2. Experimental

2.1. Materials

N-(15-Azidopentadecanoyl)-2,3,6-tri-*O*-acetyl-4-*O*-(2,3,4,6-tetra-*O*-acetyl-β-D-glucopyranosyl)-β-D-glucopyranosylamine (CTA2-C15-N_3) (M = 874.97) and *N*-(15-azidopentadecanoyl)-tri-*O*-acetyl-β-cellulosylamine (CTA13-C15-N_3, DP_n = 13) ($M_n = 4.12 \times 10^3$, $M_w = 5.33 \times 10^3$) were prepared as described in our previous articles (Kamitakahara, Enomoto, Hasegawa, & Nakatsubo, 2005; Kamitakahara & Nakatsubo, 2005). The cellulose and cellulose triacetate derivatives were abbreviated as CELL or CTA with the number of the degree of polymerization (DP_n) of the cellulosic chain (2 or 13), followed by the abbreviation of the pentadecanoyl group (C15), and the end group (N_3). MALDI-TOF MS measurements revealed that the molecular weights of CTA13-C15-N_3 with each DP value agreed well with theoretical values, and quantitative substitution of the reducing-end was confirmed. 2,2′-Azobis(isobutyronitrile) (AIBN) was crystallized from ethanol before use. 3-(Trimethyl silyl)-2-propyn-1-ol, methacryloyl chloride, triethylamine (Et_3N), *N*,*N*,*N*′,*N*′,*N*″-pentamethyldiethylenetriamine (PMDETA), copper(I)bromide (Cu(I)Br), tetrabutyl ammonium fluoride trihydrate (TBAF·$3H_2O$), and all other reagents were commercially obtained and used without further purification.

2.2. 3-(Trimethylsilyl)-2-propyn-1-yl methacrylate (TMS-PMA)

3-(Trimethylsilyl)-2-propyn-1-yl methacrylate (TMS-PMA) was prepared according to the previous article (Ladmiral et al., 2006; Scarpaci et al., 2009). To a solution of 3-(trimethylsilyl)-2-propyn-1-ol (1.0 ml, 1 eq.) and Et_3N (1.5 ml, 1.5 eq.) in dichloromethane (2.0 ml), methacryloyl chloride (1.0 ml, 1.5 eq.) was added. The mixture was stirred at room temperature for 0.5 h under nitrogen. After completion of the reaction, the mixture was extracted with ethyl acetate, washed with water and brine, dried with Na_2SO_4, and concentrated to dryness. Crude product was purified by open preparative column chromatography (eluent:ethyl acetate/*n*-hexane (1:19, v/v)) to give colorless syrup (1.12 g, 81.1% yield). ^{1}H NMR ($CDCl_3$): δ 0.20 (*CH*$_3$ (TMS)), 1.98 (*CH*$_3$), 4.78 (–O–*CH*$_2$–), 5.64, 6.20 (C=*CH*$_2$). ^{13}C NMR ($CDCl_3$): δ −0.35 (*CH*$_3$ (TMS)), 18.3 (*CH*$_3$), 52.9 (–O–*CH*$_2$–), 91.9 (–C≡*C*-TMS), 99.1 (–*C*≡C-TMS), 126.4 (*CH*$_2$=C–CH$_3$), 135.7 (CH$_2$=*C*–CH$_3$), 166.5 (*C*=O).

2.3. Poly (3-(trimethylsilyl)-2-propyn-1-yl methacrylate) (TMS-PPMA)

TMS-PMA (0.3 ml, 1 eq.) and AIBN (2.5 mg, 0.01 eq.) in benzene (0.3 ml) were loaded into a glass tube, and degassed by three freeze–pump–thaw cycles. The tube was sealed under vacuum, and placed in an oil bath at 75 °C for 1 day. The tube was cooled to room temperature, and opened. The reaction mixture was poured into methanol, filtered, and dried *in vacuo* to give an amorphous solid (158.6 mg, 58.7% yield). ^{1}H NMR ($CDCl_3$): δ 0.20 (*CH*$_3$ (TMS)), 0.95, 1.20 (*CH*$_3$), 1.85, 1.95 (*CH*$_2$), 4.60 (–O–*CH*$_2$–). ^{13}C NMR ($CDCl_3$): δ −0.24 (*CH*$_3$ (TMS)), 17.4, 19.0 (*CH*$_3$), 44.8, 45.1 (–CH$_2$–*C* (CH$_3$)–), 53.0 (–O–*CH*$_2$–), 54.3 (–*CH*$_2$–C (CH$_3$)–), 92.3 (–C≡*C*-TMS), 98.4, 98.7 (–*C*≡C-TMS), 176.1, 176.5 (*C*=O).

2.4. Poly(2-propyn-1-yl methacrylate) (PPMA)

To a solution of TMS-PPMA (128 mg) and acetic acid (50 μl. 1.5 eq. to PMA monomer unit) in tetrahydrofuran (THF) (10 ml), TBAF·$3H_2O$ was added dropwise at −20 °C. The mixture was stirred at room temperature for 3 h under nitrogen. The reaction mixture was poured into methanol. The precipitate was collected by centrifugation at 1000 rpm for 3 min, and dried *in vacuo* to give an amorphous solid (78.1 mg, 96.4% yield). The number and weight average molecular weights ($M_{n,PS}$, $M_{w,PS}$) estimated by polystyrene standards were $M_{n,PS} = 1.92 \times 10^4$ and $M_{w,PS} = 3.54 \times 10^4$, respectively. The absolute molecular weight (M_w) was calculated as 6.94×10^4 by MALS measurements. The weight average degree of polymerization (DP_w) was calculated as 5.59×10^2 from M_w(PPMA)/M(PMA) = 6.94×10^4/124.21. The DP_w of PPMA is described as $DP_w = X + Y$: X and Y are the numbers of cellulosic graft chains and PMA units of the graft copolymer (see Fig. 1). ^{1}H NMR ($CDCl_3$): δ 0.94, 1.09 (*CH*$_3$), 1.90, 1.98 (*CH*$_2$), 2.51 (–C≡*CH*), 4.62 (–O–*CH*$_2$–). ^{13}C NMR ($CDCl_3$): δ 16.9, 18.9 (*CH*$_3$), 44.8, 44.9 (–CH$_2$–*C* (CH$_3$)–), 52.2 (–O–*CH*$_2$–), 53.9 (–*CH*$_2$–C (CH$_3$)–), 75.5 (–C≡CH), 77.2 (–C≡*CH*), 175.5, 176.7 (*C*=O).

2.5. PPMA-g-(CTA2-C15)

CTA2-C15-N_3 (17.6 mg, 1 eq. to PMA monomer), PPMA (2.5 mg), and PMDETA (7 μl, 2 eq. to PMA monomer) in *N*,*N*-dimethylformamide (DMF) (0.3 ml) were loaded into a glass flask, and degassed by three freeze-pump-thaw cycles. The flask was purged with nitrogen, Cu(I)Br (5.7 mg, 2 eq. to PMA monomer) was added, and the flask was degassed again and sealed. The mixture was stirred at room temperature for 24 h. After completion of the reaction, the mixture was extracted with chloroform, washed with water and brine, dried with Na_2SO_4, and concentrated to dryness. The crude product was analyzed by SEC–MALS measurements. The compound was dried *in vacuo* to give an amorphous solid PPMA-g-(CTA2-C15) (17.8 mg, 88.6% yield). The number and weight average molecular weights ($M_{n,PS}$, $M_{w,PS}$) estimated by polystyrene standards were $M_{n,PS} = 7.58 \times 10^4$ and $M_{w,PS} = 2.24 \times 10^5$, respectively. The absolute molecular weight (M_w) was determined to be 4.22×10^5 by MALS measurements. Number of graft chains (X) was calculated as $X = 4.03 \times 10^2$ from $X = (M_w(\text{PPMA-g-(CTA2-C15)}) - M_w(\text{PPMA}))/M(\text{CTA2-C15-N}_3) = (4.22 \times 10^5 - 6.94 \times 10^4)/874.97$. Number of PMA units ($Y$) was calculated as $Y = 1.56 \times 10^2$ from $Y = DP_w(\text{PPMA}) - X = 5.59 \times 10^2 - 4.03 \times 10^2$. ^{1}H NMR ($CDCl_3$): δ 1.24 (br. s, aliphatic-H), 1.99, 2.01, 2.03, 2.04, 2.09, 2.11 (*CH*$_3$–CO), 3.72 (C5′-H, C5-H), 3.78 (C4-H), 4.01–4.17 (C6′-H$_b$, C6-H$_b$), 4.04, 4.16, 4.40, 4.44, 4.46 (C6′-H$_a$, C6-H$_a$), 4.57 (C1′-H), 4.84 (C2-H), 4.93 (C2′-H), 5.09 (C4′-H), 5.17 (C3′-H), 5.23 (C1-H), 5.27 (C3-H), 6.67 (NH), 7.93 (triazole). ^{13}C NMR ($CDCl_3$): δ 18.3 (CH$_3$), 20.4, 20.6, 20.8 (*CH*$_3$–CO–), 25.1 (C1–NH–CO–*CH*$_2$–*CH*$_2$–), 26.5, 29.2, 29.6, 30.3 (aliphatic-C), 36.4 (C1–NH–CO–*CH*$_2$–), 44.7 (CH$_2$–*C*), 50.4 (CH$_2$–O), 58.3 (CH$_2$–C), 61.5 (C6′), 61.9 (C6), 67.8 (C4′), 70.8 (C2), 71.5 (C2′), 71.8 (C5′), 72.5 (C3), 72.9 (C3′), 74.6 (C5), 77.9 (C1), 100.6 (C1′), 124.4 (CH (triazole)), 141.6 (C (triazole)), 169.1, 169.3, 169.5, 170.2, 170.3, 170.5, 171.0 (CH$_3$–*CO*–), 173.7 (C1–NH–*CO*–), 176.1, 177.1 (CO).